Journal of Computational Physics **172,** 841–878 (2001)
doi:10.1006/jcph.2001.6861, available online at http://www.idealibrary.com on IDEAL®

The Hybrid Method for the PDF Equations of Turbulent Reactive Flows: Consistency Conditions and Correction Algorithms

Metin Muradoglu, Stephen B. Pope, and David A. Caughey

Sibley School of Mechanical and Aerospace Engineering, Cornell University, Ithaca, New York 14853
E-mail: metinm@mae.cornell.edu, pope@mae.cornell.edu, caughey@mae.cornell.edu

Received September 27, 2000; revised May 25, 2001

The hybrid method solves the modeled transport equation for the joint PDF of velocity, turbulence frequency, and compositions for turbulent reactive flows. A finite-volume (FV) method is used to solve the mean conservation equations for mass, momentum, and energy and the mean equation of state; and a particle method is used to solve the modeled PDF equation. The method is completely consistent at the level of the governing equations solved by the FV and particle algorithms. In this work, the conditions to be fulfilled for full consistency at the numerical solution level are examined and the independent consistency conditions are identified. Then correction algorithms are developed to enforce these independent consistency conditions to achieve full consistency at the numerical solution level. In addition, a new formulation of the energy equation and the equation of state is developed which is both general and simple. The hybrid method is applied to a non-premixed piloted-jet flame. The numerical results show that the correction algorithms are completely successful in achieving consistency. The convergence of the method is demonstrated and, in particular, it is shown that the bias error is dramatically reduced (compared to that in previous PDF calculations). In addition, the results are shown to be in a good agreement with some earlier PDF calculations and also with the available experimental data. Because of the substantially reduced numerical error (for given grid size and number of particles), the present hybrid method represents a significant advance in the computational efficiency of particle/mesh method for the solution of PDF equations.

Key Words: hybrid finite-volume/particle method; PDF method; consistency conditions; correction algorithms.

1. INTRODUCTION

The main advantage of the joint PDF approach over conventional moment-closure methods is its ability to represent the important processes of convection and finite-rate

0021-9991/01 $35.00

non-linear reaction exactly [14, 15] without any modeling assumptions. In particular, the exact treatment of the non-linear chemical reaction makes PDF methods very attractive for simulation of complex turbulent reactive flows of practical interest [15]. However, application of the PDF method to these flows requires the development of efficient numerical solution algorithms [23]. Considerable progress has been recently made in this direction by the development of the consistent hybrid method [7, 12].

In PDF methods, turbulent closure is achieved through a modeled transport equation for the one-point, one-time joint PDF of selected fluid properties in a turbulent flow [14, 20]. The resulting modeled PDF transport equation has a completely different structure from traditional moment-closure model equations, being a high dimensional scalar equation. Thus, traditional numerical techniques such as finite-volume and finite-difference methods are not suitable to solve the PDF transport equation since the computational cost increases exponentially with the number of dimensions in these methods. On the other hand, the Monte Carlo method has proven to be a very useful tool to solve such high dimensional equations as the computational cost increases only linearly with the number of dimensions. For this reason the Monte Carlo method traditionally has been used to solve the PDF equations. In this method, the PDF is represented by an ensemble of particles [13] whose properties evolve according to model stochastic differential equations such that, ideally, the particles exhibit the same PDF as occurs in the turbulent flows they are modeling.

Several mean fields are required to close the PDF model equations. In the stand-alone particle/mesh method (such as that implemented in the PDF2DV code [17]), these mean fields are extracted directly from the particle properties. The ability of the PDF2DV code to solve the modeled PDF equations has been demonstrated, but it suffers from some deficiencies mainly caused by the statistical fluctuations in the particle mean fields [19, 23, 24]. To overcome these deficiencies, a consistent hybrid finite-volume (FV)/particle method has been developed and shown to be superior to the stand-alone particle/mesh method in terms of numerical efficiency [7, 12]. The numerical properties of the loosely coupled (present) hybrid algorithm have been extensively examined by Muradoglu *et al.* [12] in the simpler setting of 1D reactive stochastic ideal flow and it also has been successfully applied to a non-reacting bluff-body flow [8]. Since the coupling of the finite-volume and particle methods makes an important distinction between different hybrid algorithms, parallel work has been carried out to examine a more tightly coupled hybrid algorithm which has also been successfully applied to a reacting piloted-jet flame [7] and to a non-reacting bluff-body flow [8].

In the present hybrid method, several mean fields are represented as duplicate fields in the FV and particle algorithms, which raises questions of consistency. It is emphasized here that, in contrast to some earlier hybrid methods [2, 3], the present hybrid method is completely consistent at the level of equations solved by the FV and particle algorithms; that is, if the equations are solved exactly, the duplicate fields are identical. However, inconsistencies may arise at the numerical solution level due to accumulation of numerical errors. Only two conditions are identified by Muradoglu *et al.* [12] as the independent consistency conditions to be satisfied at the numerical solution level for full consistency. However, it is shown here that in fact three independent consistency conditions are required, and correction algorithms are devised to enforce these conditions to make the hybrid method fully consistent at the numerical solution level. It is found that the correction algorithms are robust and perform very well.

A simple formulation is developed to implement the general ideal gas equation of state and to evaluate the chemical source term in such a way that the mean conservation equations

solved by the FV scheme correspond to those of an ideal gas with a fixed ratio of specific heats. This leads to substantial simplification of the equations without loss of generality.

The method is implemented in the HYB2D code and tested for a non-premixed piloted-jet flame of methane [10]. The non-premixed piloted-jet flame is chosen as a test case since it has been previously studied by using the same PDF model with the stand-alone particle/mesh method (PDF2DV) and with the tightly coupled, consistent hybrid method (PDF-2D-FV) as numerical solution algorithms. Furthermore there are comprehensive experimental data available for this flame [10]. Since a primary purpose of this study is to validate the present hybrid method for reacting turbulent flows in terms of numerical accuracy and efficiency compared to the other PDF solution algorithms, the same turbulence and combustion models are used in all the simulations as in Xu and Pope [23] and Jenny *et al.* [7].

In the next section, the thermochemistry and the joint velocity–frequency-compositions PDF model employed here are briefly reviewed and the governing equations solved by the FV and particle algorithms are described. In Section 3, the consistency conditions are discussed and the independent consistency conditions are identified. Then the velocity, position, and energy correction algorithms required to achieve the full consistency at the numerical solution level are presented in Section 4, and an analysis of the position correction algorithm is presented separately in the Appendix. The numerical solution procedure and the time-averaging algorithm are described in Section 5. The test case of the non-premixed piloted-jet methane-air flame is briefly described, and the present results are compared with experimental data and with the earlier PDF calculations in Section 6, where the performance of the correction algorithms is also evaluated and presented. Finally, conclusions are drawn in Section 7.

2. GOVERNING EQUATIONS

2.1. Thermochemistry

A crucial aspect of the hybrid approach is the treatment of the equation of state and of the thermochemical energy variable. A novel approach is presented here which is both simple and general, and which involves several new energy variables.

We consider an ideal gas mixture consisting of n_s species, the thermochemical state of which is characterized by the pressure p and the set of $n_\phi = n_s + 1$ composition variables

$$\phi \equiv \{Y_1, Y_2, \ldots, Y_{n_s}, h\}, \tag{1}$$

where $\mathbf{Y}$ are the mass fractions and h is the enthalpy. The temperature T can be determined from the compositions ϕ.

The variable $\mathcal{E}(\phi)$ (which has dimensions of energy and is independent of pressure) is defined by

$$\mathcal{E}(\phi) = \mathcal{R}T \sum_\alpha \frac{Y_\alpha}{W_\alpha}, \tag{2}$$

where $\mathcal{R}$ is the universal gas constant and W_α is the molecular weight of species α. The variable $\mathcal{E}(\phi)$ is thus defined so that the equation of state is simply

$$\frac{p}{\rho} = \mathcal{E}(\phi), \tag{3}$$

and its mean is

$$\frac{\langle p\rangle}{\langle\rho\rangle} = \widetilde{\mathcal{E}(\phi)} \equiv \frac{\langle\rho\mathcal{E}(\phi)\rangle}{\langle\rho\rangle}. \tag{4}$$

For a homogeneous, adiabatic system, in the absence of mixing, the compositions evolve by

$$\frac{d\phi_\alpha}{dt} = S_\alpha(p,\phi), \quad \alpha = 1, 2, \ldots, n_s \tag{5}$$

and

$$\frac{dh}{dt} = \frac{1}{\rho}\frac{dp}{dt} = \frac{\mathcal{E}(\phi)}{p}\frac{dp}{dt}, \tag{6}$$

where $S_\alpha(p,\phi)$ is the net chemical reaction rate of species α. In applying these equations to turbulent reactive flows we neglect pressure fluctuations, so that Eqs. (5) and (6) become

$$\frac{d\phi_\alpha}{dt} = S_\alpha(\langle p\rangle,\phi), \quad \alpha = 1, 2, \ldots, n_s \tag{7}$$

and

$$\frac{dh}{dt} = \frac{\mathcal{E}(\phi)}{\langle p\rangle}\frac{d\langle p\rangle}{dt}. \tag{8}$$

In the PDF equations and particle method, the fundamental variables are $\langle p\rangle$ and ϕ, and the only thermochemical properties that are required are the reaction rates $\mathbf{S}(\langle p\rangle,\phi)$ and the variable $\mathcal{E}(\phi)$. Given $\langle p\rangle$ and $\mathcal{E}(\phi)$, the density is obtained from the equation of state: $\rho = \langle p\rangle/\mathcal{E}(\phi)$.

In the FV algorithm, the thermochemical variables are the mean pressure $\langle p\rangle$ and density $\langle\rho\rangle$, and mean *equivalent energy*, $\tilde{\epsilon}_s$.

To motivate and interpret the definition of the equivalent energy ϵ_s, we consider a calorically perfect, single component, diatomic ideal gas. The (mass-based) constant specific heats are denoted by C_{v_0} and C_{p_0}; their ratio is $\gamma_0 \equiv C_{p_0}/C_{v_0} = 1.4$, and their difference is the gas constant $R_0 = \mathcal{R}/W = C_{p_0} - C_{v_0}$. The sensible internal energy is defined by

$$\epsilon_{s_0} \equiv C_{v_0}T, \tag{9}$$

and for this case the equation of state (Eq. (3)) becomes

$$\frac{p}{\rho} = \mathcal{E} = R_0T = (\gamma_0 - 1)\epsilon_{s_0}. \tag{10}$$

Returning now to the general case, we define the equivalent energy ϵ_s by

$$\epsilon_s \equiv \frac{\mathcal{E}(\phi)}{\gamma_0 - 1}. \tag{11}$$

It may be seen that this energy is equivalent to the sensible internal energy of a calorically perfect diatomic gas at the same pressure and density. Using Eq. (3), the equivalent energy

can be alternatively expressed as

$$\epsilon_s = \frac{1}{\gamma_0 - 1}\frac{p}{\rho}. \tag{12}$$

The *equivalent enthalpy* is then defined as

$$h_s \equiv \epsilon_s + \frac{p}{\rho} = \gamma_0 \epsilon_s = \frac{\gamma_0}{\gamma_0 - 1}\mathcal{E}. \tag{13}$$

It is emphasized that although $\gamma_0 = 1.4$ is used in these definitions, the treatment of the ideal-gas thermochemistry is quite general: there is no assumption of constant specific heats.

2.2. Joint PDF Formulation

The one-point, one-time, mass-weighted joint PDF of velocity $\mathbf{U} = (U_1, U_2, U_3)^T$ and compositions $\boldsymbol{\phi} = (\phi_1, \phi_2, \ldots, \phi_{n_\phi})^T$ at location $\mathbf{x}$ and time t is defined as

$$\langle\rho\rangle \tilde{f}'(\mathbf{V}, \boldsymbol{\psi}; \mathbf{x}, t) \equiv \rho(\boldsymbol{\psi})\langle\delta(\mathbf{V} - \mathbf{U})\delta(\boldsymbol{\psi} - \boldsymbol{\phi})\rangle, \tag{14}$$

where ρ is the density and $\mathbf{V} = (V_1, V_2, V_3)^T$ and $\boldsymbol{\psi} = (\psi_1, \psi_2, \ldots, \psi_{n_\phi})^T$ are the sample space variables for velocity $\mathbf{U}$ and the composition variables $\boldsymbol{\phi}$, respectively. The delta function $\delta(\mathbf{V} - \mathbf{U})$ represents the 3D delta function at $\mathbf{V} = \mathbf{U}$. The transport equation for $\tilde{f}'(\mathbf{V}, \boldsymbol{\psi}; \mathbf{x}, t)$ can be derived from the Navier–Stokes equations [14] and is given by

$$\begin{aligned}
&\frac{\partial\langle p\rangle \tilde{f}'}{\partial t} + V_j\frac{\partial\langle\rho\rangle \tilde{f}'}{\partial x_j} - \frac{\partial\langle p\rangle}{\partial x_j}\frac{\partial \tilde{f}'}{\partial V_j} + \frac{\partial}{\partial\psi_\alpha}(\langle\rho\rangle S_\alpha \tilde{f}') \\
&\quad = \frac{\partial}{\partial V_j}\left(\left\langle -\frac{\partial\tau_{ij}}{\partial x_i} + \frac{\partial p'}{\partial x_j}|\mathbf{V}, \boldsymbol{\psi}\right\rangle \tilde{f}'\right) + \frac{\partial}{\partial\psi_\alpha}\left(\left\langle \frac{\partial J_i^\alpha}{\partial x_i}|\mathbf{V}, \boldsymbol{\psi}\right\rangle \tilde{f}'\right),
\end{aligned} \tag{15}$$

where $\tilde{}$ and $\langle\rangle$ denote mass (Favre)-averaged and volume (Reynolds)-averaged means, respectively, and the angle brackets with vertical bar $\langle\cdots|\cdots\rangle$ stands for the conditional expectation. As can be seen in Eq. (14), $\tilde{f}'$ evolves in $(7 + n_s)$-dimensional space, i.e., velocity, compositions, and physical spaces plus time. All the terms on the left-hand side of Eq. (14) are in closed form and treated exactly. These terms represent the physical processes of evolution in time, transport in the physical space, transport in the velocity space due to mean pressure gradient $\frac{\partial\langle p\rangle}{\partial x_j}$, and transport in the composition space due to reaction (S_α is the net reaction rate for species α as in Eq. (5)). However, the conditional expectations on the right-hand side of Eq. (14) appear in unclosed form and need to be modeled. These unclosed terms represent the physical processes of transport in the velocity space due to the viscous stress tensor τ_{ij} and the fluctuating pressure gradient $\frac{\partial p'}{\partial x_j}$, and transport in the composition space by the molecular fluxes J_i^α (of the scalar α in direction x_i).

In the PDF method, taking a Lagrangian viewpoint, the flow is represented by a large set of particles. Then the closure is achieved by constructing a set of stochastic differential equations that govern the evolution of the particle properties in such a way that the particles exhibit the same JPDF as the one obtained from the solution of the modeled JPDF transport equation. The models for particle velocity, turbulent frequency, scalar mixing, and reaction are discussed in the following sections.

TABLE I
Model Constants

Constant	Value	Used in
C_0	2.1	SLM
C_Ω	0.6893	definition of Ω
$C_{\omega 1}$	0.65	turbulence frequency model
$C_{\omega 2}$	0.9	turbulence frequency model
C_3	1.0	turbulence frequency model
C_4	0.25	turbulence frequency model
C_ϕ	2.0	IEM mixing model

2.3. Velocity Model

Various Langevin models have been developed for the evolution of the particle velocity to account for the acceleration due to mean pressure gradient and to provide a closure for the effects of viscous dissipation and fluctuating pressure gradient. We choose here the simplest velocity model, namely the simplified Langevin model (SLM), given by

$$dU_i^*(t) = -\frac{1}{\langle\rho\rangle}\frac{\partial\langle p\rangle}{\partial x_i}\,dt - \left(\frac{1}{2}+\frac{3}{4}C_0\right)\Omega\,(U_i^*(t)-\tilde{U}_i)\,dt + (C_0\tilde{k}\Omega)^{1/2}\,dW_i, \qquad (16)$$

where

$$\tilde{k} = \frac{1}{2}\widetilde{u_i u_i} \qquad (17)$$

is the turbulent kinetic energy, and

$$\Omega \equiv C_\Omega \frac{\langle\rho^*\omega^*|\omega^*\geq\tilde{\omega}\rangle}{\langle\rho\rangle} \qquad (18)$$

is the conditional Favre-averaged turbulent frequency with ω^* being the turbulent frequency to be defined in the following section. The model constants C_0 and C_Ω are set to their standard values as shown in Table I. The final input in Eq. (16), $\mathbf{W}(t)$, represents an isotropic vector-valued Wiener process. We note that SLM is equivalent to the Rotta model at the second-moment closure level [16].

The particle position $\mathbf{X}^*$ then evolves by

$$\frac{d\mathbf{X}^*}{dt} = \mathbf{U}^*(t). \qquad (19)$$

2.4. Turbulent Frequency Model

The particle property ω^* provides the time scale needed to close Eqs. (16) and (24).[1] The stochastic model for the turbulent frequency is given by [22]

$$d\omega^*(t) = -C_3(\omega^*-\tilde{\omega})\Omega\,dt - S_\omega\Omega\omega^*(t)\,dt + (2C_3C_4\tilde{\omega}\Omega\omega^*(t))^{1/2}\,dW, \qquad (20)$$

[1] Note: The latter equation, which describes the evolution of the mixture fraction, is presented in the next section.

where W is an independent Wiener process, and the source term S_ω is defined as

$$S_\omega = C_{\omega 2} - C_{\omega 1}\frac{P}{k\Omega}, \tag{21}$$

where $P = -\widetilde{u_i u_j}\frac{\partial \tilde{U}_i}{\partial x_j}$ is the turbulent production. The model constants $C_{\omega 1}$, $C_{\omega 2}$, $C_{\omega 3}$, and C_4 are specified in Table I.

2.5. Chemistry and Mixing Models

A simple flamelet model is employed here for the treatment of chemical reactions. The flamelet model is the same as that used in several earlier PDF simulations of the non-premixed piloted-jet flame [7, 23]. In this model, the particle thermochemical state is characterized solely by the mixture fraction defined as

$$\xi = \frac{Z_i - Z_{i2}}{Z_{i1} - Z_{i2}}, \tag{22}$$

where the subscripts 1 and 2 denote fuel and oxidizers, respectively, and Z_i is the mass fraction of the element i. With this simple chemistry model, the thermochemical variables ϕ are, by assumption, uniquely related to the mixture fraction ξ. Hence in the particle method it is sufficient to represent only ξ explicitly, and then ϕ and all other thermochemical variables can be obtained from the flamelet properties (as functions of ξ). In particular, the function $\mathcal{E}$ defined by Eq. (2) simplifies to be

$$\mathcal{E}(\xi) = \frac{p_0}{\rho(\xi)}, \tag{23}$$

where p_0 is the flamelet pressure taken as 10^5 Pa and $\rho(\xi)$ is the flamelet density.

In PDF methods, the effects of molecular diffusion are described by a mixing model. Accompanying the simple chemistry model, the simplest mixing model—the interaction by exchange with the mean (IEM) model [4]—is employed here. The IEM model can be written as

$$\frac{d\phi^*}{dt} = \mathrm{S}(\phi^*) - \frac{1}{2}C_\phi\Omega(\phi^* - \tilde{\phi}^*), \tag{24}$$

where the model constant C_ϕ is given in Table I. Mixing models are crucial in PDF simulations of turbulent non-premixed flames with finite-rate kinetics, and the IEM model is known to be problematic in this respect [21]. However, IEM gives reasonably accurate results when it is used in conjunction with equilibrium or flamelet models for non-premixed flames near equilibrium [23] such as the non-premixed piloted-jet flame studied here.

This simplified thermochemistry can be represented in the general framework described in Section 2.1 by defining (for this case): $n_\phi = 1$, $\phi_1 = \xi$, and $S_1 = 0$.

2.6. Modeled JPDF Equations

With the models described above, the modeled density-weighted JPDF of velocity, turbulent frequency, and compositions is given by

$$\begin{aligned}\langle\rho\rangle\,\tilde{f}(\mathbf{V},\psi,\theta;\mathbf{x},t) &= \mathcal{F}(\mathbf{V},\psi,\theta;\mathbf{x},t) \\ &\equiv \rho(\psi)\langle\delta(\mathbf{U}-\mathbf{V})\delta(\psi-\phi)\delta(\theta-\omega)\rangle,\end{aligned} \tag{25}$$

where $\mathbf{V}$, θ, and ψ are the sample space variables corresponding to $\mathbf{U}$, ω, and ϕ, respectively.

The transport equation for $\tilde{f}(\mathbf{V}, \psi, \theta; \mathbf{x}; t)$ can be derived from Eqs. (16), (19), (20), and (24) by using the standard procedure [14] and is given by

$$\begin{aligned}\frac{1}{\langle\rho\rangle}\frac{\partial}{\partial t}(\langle\rho\rangle\tilde{f}) = &-\frac{V_i}{\langle\rho\rangle}\frac{\partial}{\partial x_i}(\langle\rho\rangle\tilde{f}) + \frac{1}{\langle\rho\rangle} + \frac{\partial\langle\rho\rangle}{\partial x_i}\frac{\partial\tilde{f}}{\partial V_i} \\ &+ \left(\frac{1}{2}+\frac{3}{4}C_0\right)\Omega\frac{\partial}{\partial V_i}[\tilde{f}(V_i-\tilde{U}_i)] + \frac{1}{2}C_0 k\Omega\frac{\partial^2\tilde{f}}{\partial V_i\partial V_i} \\ &+ \Omega\frac{\partial}{\partial\theta}(\tilde{f}\theta S_\omega) + C_3\Omega\frac{\partial}{\partial\theta}[\tilde{f}(\theta-\tilde{\omega})] + C_3C_4\Omega\tilde{\omega}\frac{\partial^2}{\partial\theta^2}(\tilde{f}\theta) \\ &- \frac{\partial}{\partial\psi_\alpha}[\tilde{f}S_\alpha] + \frac{1}{2}C_\phi\Omega\frac{\partial}{\partial\psi_\alpha}[\tilde{f}(\psi_\alpha-\tilde{\phi}_\alpha)]. \end{aligned} \tag{26}$$

As can be seen in Eq. (25), $\tilde{f}$ evolves in a high dimensional space. For example, it evolves in $(8+n_s)$-dimensional space for an unsteady problem in 3D physical space. Therefore the conventional numerical techniques such as finite difference and finite volume methods are not suitable to solve the modeled PDF transport equation since the computational cost increases exponentially with the number of dimensions. This difficulty is overcome and the PDF simulations are made feasible by the use of the Monte Carlo method in which the computational cost increases only linearly with the number of sample-space dimensions.

2.7. Mean Conservation Equations

In the hybrid method, a FV scheme is used to solve the mean conservation equations for mass, momentum, and equivalent energy, derived directly from the modeled PDF evolution equation given by Eq. (25). Multiplying Eq. (25) by $\langle\rho\rangle$ and integrating over the entire sample space yields the mean mass conservation equation given by

$$\frac{\partial}{\partial t}\langle\rho\rangle + \frac{\partial}{\partial x_i}(\langle\rho\rangle\tilde{U}_i) = 0. \tag{27}$$

Similarly, the mean momentum conservation equation is obtained by multiplying Eq. (25) by $\langle\rho\rangle V_i$, and integrating over the entire sample space, and is given by

$$\frac{\partial}{\partial t}(\langle\rho\rangle\tilde{U}_i) + \frac{\partial}{\partial x_j}(\langle\rho\rangle\tilde{U}_i\tilde{U}_j + \langle\rho\rangle\delta_{ij}) = -\frac{\partial}{\partial x_j}(\langle\rho\rangle\widetilde{u_i u_j}). \tag{28}$$

The energy conservation equation is solved for the mean *total equivalent energy*

$$e \equiv \langle\rho\rangle\tilde{E}_s \equiv \langle\rho\rangle\left(\tilde{\epsilon}_s + \frac{1}{2}\tilde{U}_i\tilde{U}_i\right), \tag{29}$$

where $\tilde{\epsilon}_s$ can be obtained by taking the mean of Eq. (12) and is given by

$$\tilde{\epsilon}_s = \frac{1}{\gamma_0 - 1}\frac{\langle p\rangle}{\langle\rho\rangle}. \tag{30}$$

Referring to Eq. (13), we define

$$h_s(\psi) = \frac{\gamma_0}{\gamma_0 - 1}\mathcal{E}(\psi). \tag{31}$$

Now multiplying Eq. (25) by $h_s(\psi)$ and integrating yields

$$\frac{\partial}{\partial t}(\langle\rho\rangle\tilde{h}_s) + \frac{\partial}{\partial x_i}(\langle\rho\rangle\tilde{h}_s\tilde{U}_i) = -\frac{\partial}{\partial x_i}(\langle\rho\rangle\widetilde{(u_i h_s'')}) + \langle\rho\rangle\widetilde{(h_{s,\alpha}S_\alpha)} - \frac{1}{2}C_\phi\langle\rho\rangle\Omega\widetilde{(\phi_\alpha'' h_{s,\alpha})}, \tag{32}$$

where $h_{s,\alpha} \equiv \frac{\partial h_s(\phi)}{\partial \phi_\alpha}$, $h_s'' \equiv h_s - \tilde{h}_s$, and $\phi_\alpha'' \equiv \phi_\alpha - \tilde{\phi}_\alpha$.

It may be noted from Eq. (24) that the equivalent enthalpy following a particle evolves by

$$\frac{dh_s^*}{dt} = h_{s,\alpha}\frac{d\phi_\alpha^*}{dt} = h_{s,\alpha}\left(S_\alpha - \frac{1}{2}C_\phi\Omega(\phi_\alpha^* - \tilde{\phi}_\alpha)\right). \tag{33}$$

Hence the final two terms in Eq. (31) can be conveniently written (and evaluated) as

$$\langle\rho\rangle\tilde{\dot{q}} = \langle\rho\rangle\left(\widetilde{\frac{dh_s}{dt}}\right), \tag{34}$$

so that Eq. (31) can be rewritten as

$$\frac{\partial}{\partial t}(\langle\rho\rangle\tilde{h}_s) + \frac{\partial}{\partial x_i}(\langle\rho\rangle\tilde{h}_s\tilde{U}_i) = \langle\rho\rangle\tilde{\dot{q}} - \frac{\partial}{\partial x_i}(\langle\rho\rangle\widetilde{u_i h_s''}). \tag{35}$$

In fact, Eq. (35) (with $\tilde{\dot{q}}$ is defined by Eq. (34)) is more general than Eq. (31), since it holds for any mixing model. As the notation implies, $\tilde{\dot{q}}$ is the heat release rate (or more precisely, the rate of addition of equivalent enthalpy) due to reaction and mixing.

Finally the evolution equation for $\langle\rho\rangle\tilde{E}_s$ can be deduced from Eqs. (27)–(29) and (35) to give

$$\begin{aligned}\frac{\partial}{\partial t}(\langle\rho\rangle\tilde{E}_s) + \frac{\partial}{\partial x_i}(\tilde{U}_i(\langle\rho\rangle\tilde{E}_s + \langle p\rangle)) \\ = \langle\rho\rangle\tilde{\dot{q}} - \frac{\partial}{\partial x_i}(\langle\rho\rangle\widetilde{u_i h_s''}) - \frac{\bar{D}\langle p\rangle}{Dt} - \tilde{U}_i\frac{\partial}{\partial x_j}(\langle\rho\rangle\widetilde{u_i u_j}),\end{aligned} \tag{36}$$

where we define

$$\frac{\bar{D}}{Dt} \equiv \frac{\partial}{\partial t} + \tilde{U}_i\frac{\partial}{\partial x_i}. \tag{37}$$

Relative to the convective terms in Eq. (35), the term $\frac{\bar{D}\langle p\rangle}{Dt}$ is of order of Ma^2, where Ma is the local Mach number and is negligible in low Mach number flows. Furthermore, the last term in Eq. (35) represents the turbulence production and it is also negligibly small compared to the chemical source term and the scalar fluxes. Therefore, to an excellent approximation, for low Mach number flows, the mean energy equation reduces to

$$\frac{\partial}{\partial t}(\langle\rho\rangle\tilde{E}_s) + \frac{\partial}{\partial x_i}(\tilde{U}_i(\langle\rho\rangle\tilde{E}_s + \langle p\rangle)) = \langle\rho\rangle\tilde{\dot{q}} - \frac{\partial}{\partial x_i}(\langle\rho\rangle\widetilde{u_i h_s''}). \tag{38}$$

Using Eqs. (29) and (30), the mean equation of state can be alternatively written as

$$\langle p\rangle = (\gamma_0 - 1)\langle\rho\rangle\left(\tilde{E}_s - \frac{1}{2}\tilde{U}_i\tilde{U}_i\right). \tag{39}$$

In summary, the FV algorithm is employed to solve the conservation equations for mean mass (Eq. (27)), the mean momentum (Eq. (28)), and the mean total equivalent energy (Eq. (35) or Eq. (38) for low Mach number flows), coupled with the mean equation of state (Eq. (39)).

It is emphasized here that all the terms appearing on the right-hand side of the mean conservation equations are supplied by the particle algorithm so that, as far as the FV method is concerned, these equations may be regarded as the compressible Euler equations with added source terms. Furthermore, these mean equations are completely consistent with the modeled PDF equation from which they are derived.

2.8. Particle System

In the context of the hybrid algorithm, the instantaneous particle velocity $\mathbf{U}^*$ is replaced by the fluctuating velocity $\mathbf{u}^* = \mathbf{U}^* - \tilde{\mathbf{U}}^*$ since the Favre-averaged mean velocity $\tilde{\mathbf{U}}^*$ is interpolated from the FV data. Therefore, the mean velocity evolution equation is subtracted from the velocity model to obtain the evolution equation for the fluctuating part. The SLM model for the fluctuating part of the velocity is given by

$$du_i^*(t) = \frac{1}{\langle\rho\rangle}\frac{\partial(\langle\rho\rangle\widetilde{u_i u_j})}{\partial x_j}\,dt - u_j^*\frac{\partial \widetilde{U}_i}{\partial x_j}\,dt - \left(\frac{1}{2}+\frac{3}{4}C_0\right)\Omega u_i^*(t)\,dt + (C_0\tilde{k}\Omega)^{1/2}\,dW_i. \tag{40}$$

The particle position $\mathbf{X}^*$ then evolves by

$$\frac{d\mathbf{X}^*}{dt} = \tilde{\mathbf{U}}^* + \mathbf{u}^*. \tag{41}$$

The particle algorithm is employed to solve the modeled PDF transport equation for the JPDF of $\mathbf{u}$, ϕ, and ω, denoted by $\tilde{g}$. The evolution equation for $\tilde{g}$ can be either derived from Eqs. (20), (24), (40), and (41) by the standard techniques [14] or directly deduced from Eq. (25) by using the relationship

$$\tilde{g}(\mathbf{v}, \psi, \theta; \mathbf{x}, t) = \tilde{f}(\tilde{\mathbf{U}} + \mathbf{v}, \psi, \theta; \mathbf{x}, t). \tag{42}$$

As a result, all the equations solved by the FV and particle algorithms are completely consistent since they are all derived from the same equation, namely the modeled PDF transport equation given by Eq. (25).

3. CONSISTENCY CONDITIONS

As discussed above, the present hybrid algorithm is completely consistent at the level of the governing equations. However, the solutions may not be consistent at the level of the numerical solutions due to the accumulation of numerical errors, and correction algorithms are required to enforce consistency of some variables.

Assuming that the FV fields are stored at cell centers representing cell averages, it is simplest to consider ensemble averages of the particles within each cell to obtain consistency at the numerical level. For cell α, the independent mean fields represented in the FV code are $\langle\rho\rangle_\alpha^{FV}$, $\langle p\rangle_\alpha^{FV}$, $\tilde{\mathbf{U}}_\alpha^{FV}$, and $\tilde{\epsilon}_{s_\alpha}^{FV}$ and we need to make sure that these quantities are consistent with the corresponding particle fields.

Each particle has a set of intrinsic properties, namely the mass m^*, the position $\mathbf{X}^*$, the fluctuating velocity $\mathbf{u}^*$, the turbulence frequency ω^* and the compositions ϕ^*, and a set of interpolated properties (interpolated from the corresponding FV fields onto particles) including the mean pressure $\langle p\rangle^*$ and the mean velocity $\tilde{\mathbf{U}}^*$. Note that the intrinsic particle properties are random and there are no underlying random fields. These intrinsic and interpolated particle properties are called the primary particle properties and contain no redundancy. However, various secondary particle properties may be derived from these primary properties such as density ρ^*, specific volume $v^* \equiv 1/\rho^*$ and the equivalent energy ϵ_s^*.

In the cell α, the indicator function $I_\alpha(\mathbf{x})$ is defined such that $I_\alpha(\mathbf{x}) = 1$ if x is in the cell, and $I_\alpha(\mathbf{x}) = 0$ otherwise. Then the geometric volume of the cell is given by

$$V_\alpha \equiv \int I_\alpha(\mathbf{x})\, d\mathbf{x}. \tag{43}$$

The total particle mass M_α^P and the mean particle volume V_α^P in the cell are

$$M_\alpha^P \equiv \sum_i m_i^* I_\alpha(\mathbf{X}_i^*), \tag{44}$$

and

$$V_\alpha^P \equiv \sum_i m_i^* v_i^* I_\alpha(\mathbf{X}_i^*), \tag{45}$$

where the summation is over all the particles. Then the particle mass density for the cell is defined as

$$q_\alpha \equiv \frac{M_\alpha^P}{V_\alpha}. \tag{46}$$

The Favre-averaged and Reynolds-averaged particle means of a particle property ϕ^* are hence defined as

$$\tilde{\phi}_\alpha^P \equiv \sum_i m_i^* \phi_i^* I_\alpha(\mathbf{X}_i^*) \big/ M_\alpha^P, \tag{47}$$

and

$$\langle\phi\rangle_\alpha^P \equiv \sum_i m_i^* v_i^* \phi_i^* I_\alpha(\mathbf{X}_i^*) \big/ V_\alpha^P. \tag{48}$$

Note that Eqs. (47) and (48) are consistent in that: for $\phi = 1$, $\tilde{1} = \langle 1\rangle = 1$. For $\phi = v$, Eq. (47) yields

$$\tilde{v}_\alpha^P \equiv V_\alpha^P \big/ M_\alpha^P, \tag{49}$$

and for $\phi = \rho$, Eq. (48) gives

$$\langle\rho\rangle_\alpha^P \equiv M_\alpha^P \big/ V_\alpha^P = 1/\tilde{v}_\alpha^P. \tag{50}$$

All of these mean particle properties are internally consistent if

$$V_\alpha^P = V_\alpha, \tag{51}$$

for then

$$\langle \rho \rangle_\alpha^P = 1/\tilde{v}_\alpha^P = q_\alpha \left(\frac{V_\alpha}{V_\alpha^P} \right) = q_\alpha. \tag{52}$$

Alternatively, we can take this consistency condition to be

$$\langle \rho \rangle_\alpha^P = q_\alpha. \tag{53}$$

Now we are in a position to examine the consistency between the FV and particle mean fields. For the mean fields represented in the FV code, the consistency conditions are identified as

$$\langle \rho \rangle_\alpha^P = \langle \rho \rangle_\alpha^{FV}, \tag{54}$$

$$\langle p \rangle_\alpha^P = \langle p \rangle_\alpha^{FV}, \tag{55}$$

$$\tilde{\mathbf{u}}_\alpha^P = 0, \tag{56}$$

$$\tilde{\epsilon}_\alpha^P = \tilde{\epsilon}_\alpha^{FV}. \tag{57}$$

Since the pressure field is interpolated from the FV data onto particles, assuming that a second-order interpolation scheme is used, the condition given by Eq. (55) is satisfied with second-order spatial accuracy; i.e.,

$$\langle p \rangle_\alpha^P = \langle p \rangle_\alpha^{FV} + \mathcal{O}(\Delta x^2), \tag{58}$$

where Δx is the grid spacing. That is, to within the truncation error of the method, Eq. (55) is automatically satisfied and does not require further consideration.

The equations of the state used in the FV and particle algorithms are

$$\langle p \rangle_\alpha^{FV} = (\gamma_0 - 1) \langle \rho \rangle_\alpha^{FV} \tilde{\epsilon}_{s_\alpha}^{FV} \tag{59}$$

and

$$\langle p \rangle_i^* = (\gamma_0 - 1) \rho_i^* \epsilon_{s_i}^*. \tag{60}$$

Now from Eqs. (60) and (48), we obtain

$$\begin{aligned} \langle p \rangle_\alpha^P &= \sum_i m_i^* v_i^* p_i^* I_\alpha(\mathbf{X}_i) / V_\alpha^P \\ &= \sum_i m_i^* (\gamma_0 - 1) \epsilon_{s_i}^* I_\alpha(\mathbf{X}_i) / V_\alpha^P \\ &= (\gamma_0 - 1) \frac{M_\alpha^P}{V_\alpha^P} \tilde{\epsilon}_{s_\alpha}^P \\ &= (\gamma_0 - 1) q_\alpha \tilde{\epsilon}_{s_\alpha}^P. \end{aligned} \tag{61}$$

Thus, if Eqs. (57) and (58) are satisfied, we obtain from Eqs. (59) and (60) (to order Δx^2)

$$q_\alpha = \langle \rho \rangle_\alpha^{FV}. \tag{62}$$

If the internal consistency condition Eq. (53) is also satisfied, then Eq. (62) leads to $\langle\rho\rangle_\alpha^P = \langle\rho\rangle_\alpha^{FV}$ (to order Δx^2). Hence if Eqs. (53), (57), and (58) are satisfied, then so also is Eq. (54). As a result, the independent consistency conditions to be satisfied at the level of the numerical solutions are identified as those given by Eqs. (53), (56), and (57). These conditions are enforced by the correction algorithms as discussed in the following section.

Note that Muradoglu *et al.* [12] identified the conditions given by Eqs. (56) and (57) as the only independent consistency conditions, and the condition given by Eq. (53) is mistakingly claimed to be a dependent consistency condition implied by Eqs. (56) and (57). The discussion above shows that claim to be incorrect.

In summary, the three independent consistency conditions that are not automatically satisfied are $\langle\rho\rangle_\alpha^P = q_\alpha$, $\tilde{\mathbf{u}}_\alpha = 0$, and $\tilde{\epsilon}_{s_\alpha}^P = \tilde{\epsilon}_{s_\alpha}^{FV}$. Of the other consistency conditions, $\langle p\rangle_\alpha^P = \langle p\rangle_\alpha^{FV}$ is automatically satisfied (to within the truncation error), while $\langle\rho\rangle_\alpha^P = \langle\rho\rangle_\alpha^{FV}$ and $V_\alpha^P = V_\alpha$ are dependent upon the three independent conditions. Thus satisfaction of the three independent conditions is sufficient to ensure the consistency of the method at the numerical level.

4. CORRECTION ALGORITHMS

In this section, we describe velocity, position, and energy correction algorithms which enforce the independent consistency conditions at the numerical solution level. The velocity correction algorithm corrects $\mathbf{u}^*$ to enforce the condition $\tilde{\mathbf{u}}^P = 0$, the position correction algorithm corrects $\mathbf{X}^*$ to enforce the condition $q = \langle\rho\rangle^P$, and the energy correction algorithm corrects $\tilde{\epsilon}_s^{FV}$ to enforce $\tilde{\epsilon}_s^{FV} = \tilde{\epsilon}_s^P$. (Henceforth we simplify the notation by omitting the subscript α denoting the cell.)

It is stressed that only statistically stationary flows are considered and that all the correction algorithms are designed to impose the required conditions only at this stationary state.

4.1. Velocity Correction Algorithm

The consistency condition given by Eq. (56) states that the expectation of the fluctuating velocity remains zero. This condition is not automatically satisfied due to accumulation of numerical errors, so it is enforced using the simple correction algorithm proposed by Jenny *et al.* [7]. In this method, before the correction, the mean fluctuating velocity is extracted from the particles by using the kernel estimation technique [5, 6], and the result is denoted by $\tilde{\mathbf{u}}_{bc}^*$. It is then time-averaged (denoted by $\tilde{\mathbf{u}}_{bc,TA}^*$), and the correction is performed (on each time step) by subtracting $\tilde{\mathbf{u}}_{bc,TA}^*$ from the particle fluctuating velocity $\mathbf{u}^*$. The algorithm may be summarized as

$$\mathbf{u}^* = \mathbf{u}_{bc}^* - \tilde{\mathbf{u}}_{bc,TA}^*, \tag{63}$$

where the value $\tilde{\mathbf{u}}_{bc,TA}^* = \tilde{\mathbf{u}}_{bc,TA}(\mathbf{X}^*)$ is interpolated from the time-averaged mean fluctuating velocity field stored at cell vertices.

Taking the Favre-average of both sides of Eq. (63) and time-averaging over a long time scale yields

$$\tilde{\mathbf{u}}_{TA}^* = \mathcal{O}(\Delta x^2), \tag{64}$$

showing that the required condition is satisfied to within the spatial truncation error stemming from the kernel estimation and interpolation operations. Note that the condition could be satisfied exactly if $\tilde{\mathbf{u}}^*$ were evaluated by an ensemble average in each cell representing the cell average.

4.2. Position Correction Algorithm

The position correction is performed to correct the particle position $\mathbf{X}^*$ to enforce the condition $q_{TA} = \langle\rho\rangle^P_{TA}$, where q_{TA} and $\langle\rho\rangle^P_{TA}$ are the time-averaged mean particle mass density and the particle mean density, respectively. The condition is effected through a correction velocity $\mathbf{U}^c(\mathbf{x}, t)$, so that particles move with the velocity $\tilde{\mathbf{U}}(\mathbf{X}^*, t) + \mathbf{U}^c(\mathrm{X}^*, t) + \mathbf{u}^*(t)$.

The algorithm works by driving the normalized density difference (for each cell)

$$Q \equiv \frac{q - \langle\rho\rangle}{\langle\rho\rangle_{TA}} \tag{65}$$

to zero in a time-averaged sense when a statistically steady state is reached. The algorithm also involves the smoothed density difference $\bar{Q}(\mathrm{x}, t)$ which is obtained by solving the equation

$$\frac{\partial \bar{Q}}{\partial t} = -(\bar{Q} - Q)c\frac{U_o}{L} + fU_oL\frac{\partial^2 \bar{Q}}{\partial x_i \partial x_i}, \tag{66}$$

by a FV method. Here U_o and L are velocity and length scales, and c and f are nondimensional parameters, all to be specified. Observe that Eq. (66) is a time-averaging operator with an additional diffusive term, so that the quantity $\bar{Q}$ is Q smoothed both in time (over the time-averaging time scale $\tau^c_{TA} = \frac{L}{U_o c}$) and in space. The final quantity used in the algorithm is a correction potential ϕ that evolves by

$$\frac{\partial \phi}{\partial t} = bU_o^2 Q, \tag{67}$$

where b is a non-dimensional parameter to be specified. Then the correction velocity is specified as

$$U_i^c = -\frac{\partial \phi}{\partial x_i} - aU_oL\left[\zeta\frac{\partial \bar{Q}}{\partial x_i} + (1-\zeta)\frac{\partial Q}{\partial x_i}\right] \tag{68}$$

$$\zeta = \begin{cases} 1 & \text{if } \dfrac{\langle q\rangle}{\langle\rho\rangle} \geq \epsilon_\zeta \\ 0 & \text{if } \dfrac{\langle q\rangle}{\langle\rho\rangle} < \epsilon_\zeta, \end{cases} \tag{69}$$

where a is again a non-dimensional parameter to be specified, ζ is a switching function that replaces $\bar{Q}$ with Q to allow the algorithm to respond quickly when the mass density is too small compared to the particle mean density, and ϵ_ζ is a free parameter to be specified.

The algorithm depends on ϕ attaining a statistically stationary state. For then the time average of Eq. (67) yields

$$Q_{TA} = 0, \tag{70}$$

and hence

$$\langle q \rangle_{TA} = \langle \rho \rangle_{TA}. \tag{71}$$

Therefore, the consistency condition is satisfied exactly in a time-averaged sense when a statistically stationary state is reached.

The questions remain: Does ϕ become statistically stationary? How should the parameters be chosen to attain the statistically stationary state quickly and with small fluctuations? These questions are addressed in the Appendix. Based on the analysis presented in the Appendix and experience with the algorithm, the parameters are specified as

$$L = \frac{\Delta x}{\pi} \tag{72}$$

$$U_o = |U|_{\max} \tag{73}$$

$$c = \frac{1}{\pi} \frac{1}{(CFL)_P N_{TA}^c} \tag{74}$$

$$f = k_f c \tag{75}$$

$$b = k_b f = k_b k_f c \tag{76}$$

$$a = \left(1 + \frac{b}{c^2}\right), \tag{77}$$

where Δx is the characteristic spatial grid size and $|U|_{\max}$ is the maximum mean velocity in the computational domain. The parameters k_f, k_b, N_{TA}^c, $(CFL)_P$, and ϵ_ζ are typically taken as 3, 8, 20, 0.4, and 0.25, respectively.

4.3. Energy Correction Algorithm

The consistency condition given by Eq. (57) states that the Favre-averaged mean FV and particle energy fields are equal, and it is again not automatically satisfied at the numerical solution level. Since the thermochemistry is provided by the particle algorithm, the particle mean energy field is inherently more accurate than the corresponding FV field. Therefore, a correction is performed on the FV field to require that it relax to the particle field.

The energy conservation equation can be written as

$$\frac{\partial e^{FV}}{\partial t} = G, \tag{78}$$

where e^{FV} is defined as

$$e^{FV} = \langle \rho \rangle^{FV} \left(\tilde{\epsilon}_s^{FV} + \frac{1}{2} \tilde{\mathbf{U}}^{FV} \cdot \tilde{\mathbf{U}}^{FV} \right), \tag{79}$$

and G represents all the remaining terms in the mean energy equation (Eq. (35) or Eq. (38)). The consistency condition can be also expressed alternatively as

$$e^{FV} = e^P, \tag{80}$$

where

$$e^P = \langle\rho\rangle^P \left(\tilde{\epsilon}_s^P + \frac{1}{2}\tilde{\mathbf{U}}^{FV} \cdot \tilde{\mathbf{U}}^{FV} \right). \tag{81}$$

The correction algorithm is then specified as[2]

$$\frac{\partial e^{FV}}{\partial t} = G + F + 2 f_e \Omega_F (e^P - e^{FV}), \tag{82}$$

and

$$\frac{\partial F}{\partial t} = \Omega_F^2 (e^P - e^{FV}), \tag{83}$$

where F is a forcing term, and f_e and Ω_F are positive real constants. In the statistically stationary state, the consistency condition is satisfied since the long time average of Eq. (83) yields

$$e_{TA}^P = e_{TA}^{FV}. \tag{84}$$

These equations can be readily analyzed to determine appropriate choices of the parameters f_e and Ω_F. Differentiating Eq. (83) with respect to time and using Eq. (82) leads to

$$\frac{\partial^2 F}{\partial t^2} + 2 f_e \Omega_F \frac{\partial F}{\partial t} + \Omega_F^2 F = -\Omega_F^2 G, \tag{85}$$

which is in the same form as the equation for a mass-spring-damper system with the natural frequency Ω_F and damping coefficient f_e. Therefore, a value of f_e around unity can be expected to produce satisfactory behavior. In the calculations reported below, the parameter f_e is taken to be 1.05 and the specification of the remaining parameter Ω_F is discussed in Section 6.2.3.

As the above analysis shows, e^{FV} should relax smoothly to the particle field e^P to satisfy the required consistency condition if the equations are solved accurately. However, a numerical ill-conditioning arises in solving Eqs. (82) and (83) since the total energy e^{FV} varies very little over the flow field even if $\tilde{\epsilon}_s^{FV}$ varies by factor of 7 or more. This difficulty is easily circumvented by replacing the mean particle density $\langle\rho\rangle^P$ in Eq. (81) with the mean FV density $\langle\rho\rangle^{FV}$ so that the final form of the correction algorithm becomes

$$\frac{\partial e^{FV}}{\partial t} = G + F + 2 f_e \Omega_F \langle\rho\rangle^{FV} \left(\tilde{\epsilon}_s^P - \tilde{\epsilon}_s^{FV} \right), \tag{86}$$

and

$$\frac{\partial F}{\partial t} = \Omega_F^2 \langle\rho\rangle^{FV} \left(\tilde{\epsilon}_s^P - \tilde{\epsilon}_s^{FV} \right). \tag{87}$$

It should be noted that Eq. (87) does not contain any spatial derivatives and it can be solved independently for each cell, separately from the rest of the equations solved by the FV scheme.

[2] Note: The correction algorithm is written in this form to facilitate a simple analysis. The final form of the algorithm is given by Eqs. (86) and (87).

It is also important to note that the specification of G in Eqs. (82) and (86) is immaterial to the satisfaction of the consistency condition and to the resulting values of e^{FV} and $\tilde{\epsilon}_s^{FV}$ (although it does affect the transient behavior). Hence it is unnecessary to implement G in full as given by Eq. (35) or Eq. (38). Therefore, since the particle fields may contain large statistical fluctuations that may lead to a stability problem in the FV algorithm, only the chemical source term is retained and all the other terms are removed from the right-hand side of Eq. (35). Even though the chemical source term is also extracted from the particles, it contains relatively small statistical fluctuations compared to the scalar fluxes so that it is retained to improve the convergence rate of the FV algorithm. As a result, the energy correction algorithm may be considered as a smoothing operator which reduces the statistical fluctuations in $\tilde{\epsilon}_s^P$ to be used in the FV algorithm.

5. NUMERICAL SOLUTION PROCEDURE

The loosely coupled consistent hybrid FV/particle method [12] is used here to solve the PDF equations. In this approach, a FV scheme is employed to solve the mean conservation equations for the mass, momentum, and energy, coupled with the mean equation of state, while a particle/mesh method is used to solve the modeled transport equation of the JPDF for the fluctuating velocity, turbulent frequency, and compositions. It is stressed here again that, in contrast to some earlier hybrid algorithms [2, 3], the equations solved by the present hybrid method are fully consistent. The particle and FV codes are linked to close the particle evolution and RANS equations as follows. The mean velocity and pressure fields are provided to the particle code by the FV code while the FV code gets all the Reynolds stresses, the chemical source term, and $\tilde{\epsilon}_s^P$ from the particles. As shown by Muradoglu *et al.* [12] and Jenny *et al.* [7], the statistical error is substantially reduced in the mean velocity and pressure fields in the hybrid method compared to the stand-alone particle/mesh method. It has also been shown that the use of these smooth fields in the particle evolution equations leads to a dramatic reduction in the deterministic bias error [7, 12].

In the solution process, the FV and particle methods are periodically used to solve their respective equations. The form of coupling between the FV and particle algorithms distinguishes different hybrid methods. In this study a pseudo loosely coupled algorithm has been adopted in which an outer iteration is completed by running the FV and particle codes each for a specified number of time steps. In the initial stages of the solution, both the FV and particle codes are run for relatively few time steps in each outer iteration; typically, the FV and particle codes are run for 10 and 5 time steps, respectively. As the solution approaches a statistically stationary state, the number of time steps taken in each FV and particle inner iteration is gradually increased and finally set to their specified maximum value, typically 40 and 10 for the FV and particle codes, respectively. A similar strategy is also applied to the time-averaging scheme; i.e., the time-averaging time scale is initially chosen to be relatively small and is gradually increased up to its specified maximum value as the solution approaches the statistically stationary state. In this way, global convergence is attained more quickly due to the increased interaction between the two codes and the use of less time-averaging in the transient regime; the desired smooth solutions are then recovered by using a more loosely coupled strategy and longer time-averaging as the solution nears a stationary state.

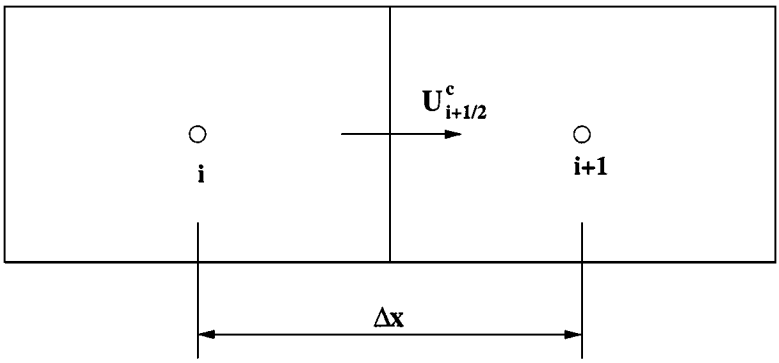

FIG. 1. A sketch of typical cells showing the evaluation of the correction velocity component in the x direction used in the position correction algorithm.

Since the hybrid algorithm is designed to treat only steady flows, the time steps taken in the FV and particle inner iterations need not be the same and are specified separately according to the stability and accuracy criteria of the respective algorithms.

Such a pseudo loosely coupled hybrid algorithm has been implemented in the HYB2D code [8]. In this code, the particle algorithm is essentially based on the PDF2DV code [17], while the FV scheme is a slight modification of that developed by Caughey [1]. The details of the complete algorithm can be found in [8, 12].

For the position correction algorithm, the mean particle mass density q and the particle mean density $\langle\rho\rangle$ are evaluated at cell centers as ensemble means. The position correction potential ϕ, the smoothed density difference $\bar{Q}$, and the density difference Q are also evaluated and stored at cell centers. The spatial derivatives in Eqs. (66) and (68) are approximated by second-order central differences. Equations (66) and (67) are advanced in time by an explicit Euler method for a single time step at each particle time step. The same time step is used as that used to advance the particle equations. As sketched in Fig. 1, the correction velocity for the position correction is evaluated at the cell faces and then interpolated on the particles using the same interpolation scheme as for the mean convective velocity. The spatial derivatives needed to calculate the correction velocity are also approximated by second-order central differences.

As remarked before, Eq. (87) in the energy correction algorithm does not contain any spatial derivatives. In the solution process, it is decoupled from the system of mean conservation equations and advanced separately by using an explicit Euler method at each FV time step. Note that the particle field $\tilde{\epsilon}_s^P$ used in the energy correction algorithm is also evaluated at the cell centers as an ensemble mean.

5.1. Time-Averaging Method

Time-averaging is a powerful tool to reduce the statistical error in the particle mean fields for a fixed number of particles [23]. The time-averaging method employed here is different from that proposed by Muradoglu *et al.* [12] and is defined, for a particle mean field Q, as

$$Q^k_{TA} = \left(1 - \frac{1}{N_{TA}}\right) Q^{k-1}_{TA} + \frac{1}{N_{TA}} Q^k, \tag{88}$$

where Q^k_{TA} and Q^k are the time-averaged and instantaneous values evaluated at kth particle time step. The parameter N_{TA} is a time-averaging factor to be specified.

In the case of the Favre-averaged mean fields, the numerators and dominator are time-averaged separately. For example, the time-averaged counterpart of the mean field defined by Eq. (47) is evaluated as

$$(\tilde{\phi}_\alpha)_{TA} = \frac{\left(\sum_i m_i^* \phi_i^* I_\alpha(\mathbf{X}_i^*)\right)_{TA}}{\left(\sum_i m_i^* I_\alpha(\mathbf{X}_i^*)\right)_{TA}}. \tag{89}$$

This way of time-averaging has the advantage of being very robust against the cases of empty cells or cells with a small number of particles.

6. RESULTS AND DISCUSSION

6.1. Model Problem—Masri and Bilger's Flame L

The test problem chosen is an axisymmetric, non-premixed piloted-jet flame studied experimentally by Masri *et al.* [10]. The same flame has also been chosen as a test case in several earlier PDF simulations [7, 23]. The details of the burner used in the experiments are provided by Masri *et al.* [10]. An axisymmetric jet of methane fuel with radius $R_j = 3.6$ mm is centered in an annular pilot with radius $R_p = 9.0$ mm. The pilot burns a mixture of stoichiometric composition ($\xi = \xi_s = 0.055$) and provides a heat source which stabilizes the main jet at the exit plane. The flame is surrounded by an unconfined coflow stream of air. The bulk velocities in the jet, in the pilot, and in the coflow are specified to be $U_j = 41$ m/s, $U_p = 24$ m/s, and $U_c = 15$ m/s, respectively. These conditions correspond to Flame L of Masri and Bilger [11]. Measurements have been performed for temperature by the thermocouple method, velocity by LDA and compositions by sample probes. Experimental data are published by Masri *et al.* [10] and are also available at the Web site of the University of Sydney [9].

6.2. Results

The primary purpose of the present work is to validate the consistent hybrid method for reacting turbulent flows in terms of numerical accuracy and efficiency compared to the other PDF solution algorithms [7, 23] and to evaluate the performance of the correction algorithms in achieving consistency at the numerical level. Therefore, the same grids, the same initial and boundary conditions, and the same turbulence and chemistry models are used here as were used by Xu and Pope [23] and by Jenny *et al.* [7]. The inlet boundary conditions, which are also used as initial conditions, are shown in Fig. 2.

For the numerical simulation, a cylindrical coordinate system is adopted with the origin of the radial coordinate (r) placed at the center of the fuel jet. Following Xu and Pope [23], the computational domain is taken to be $80R_j$ long in the axial direction (x) and extends to $15R_j$ in the radial direction. The domain is divided into a total of M^2 non-uniform grid cells, where M is between 20 and 64. The details of the computational grid and the initial and boundary conditions can be found in [23].

For the FV method, the mean velocity and density are fixed at the inlet boundary, while the pressure is extrapolated from the computational domain. At the outlet boundary, the mean velocity and density are extrapolated from the computational domain and pressure is

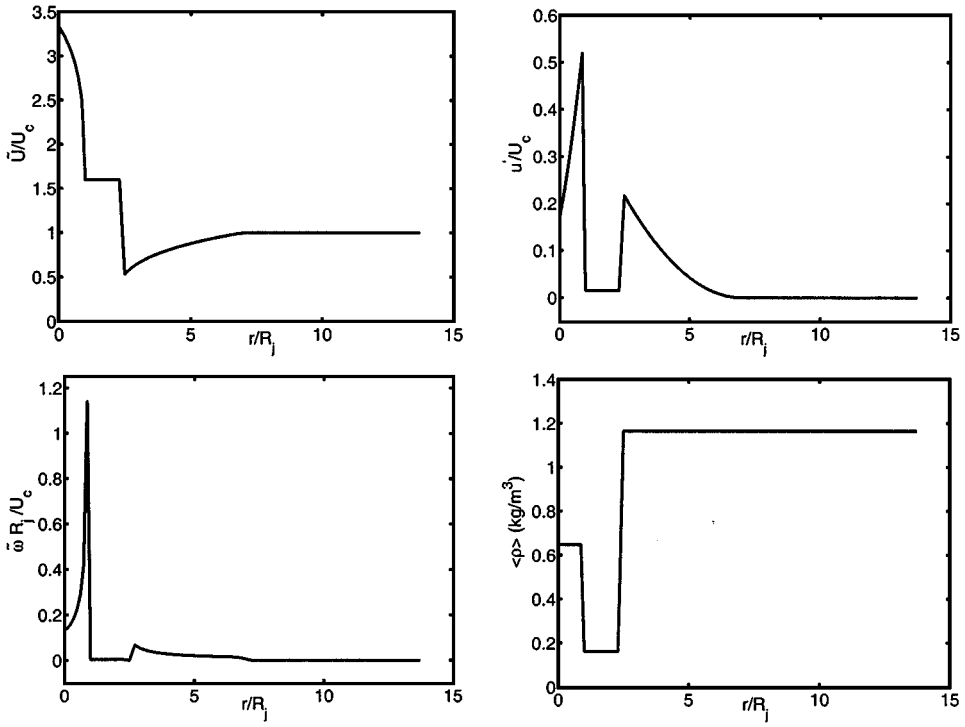

FIG. 2. Inlet profiles of the normalized mean axial velocity, the normalized rms axial fluctuating velocity, the normalized turbulent frequency, and the mean density for flame L.

fixed to the pressure calculated as

$$p = p_0 - \langle\rho\rangle\widetilde{vv}, \tag{90}$$

where p_0 is the atmospheric pressure ($p_0 = 10^5$ Pa) and v is the fluctuating velocity in the radial direction evaluated at the outlet boundary. We note that Eq. (90) is exact for plane flows but is only approximately correct for axisymmetric flows, involving the assumption that fluctuating velocities in the radial and circumferential directions are equal [20].

Results are now presented for the hybrid method implemented in the HYB2D code applied to simulate the non-premixed piloted-jet flame, flame L. The statistical stationarity of the numerical solution is first inspected. Then the Favre-averaged mean velocity and mixture fraction profiles at $40R_j$ downstream of the nozzle are compared with the experimental data and with the earlier PDF simulations to verify the accuracy of the present algorithm. The internal consistency and performance of the correction algorithms are also investigated. Finally the spatial discretization (grid convergence) and bias errors are studied and compared with those of the other PDF solution algorithms.

In Fig. 3, the Favre-averaged mean axial velocity and mean mixture fraction profiles are shown at $40R_j$ downstream of the nozzle and compared with the experimental data [10] and with the earlier results of PDF simulations by Xu and Pope [23] using the stand-alone particle/mesh method and by Jenny *et al.* [7] using the tightly coupled consistent hybrid method.

The results of all three simulations are obtained on the same 40×40 grid, 200 particles per cell are used in PDF2DV, while 160 particles per cell are used in HYB2D (present) and in

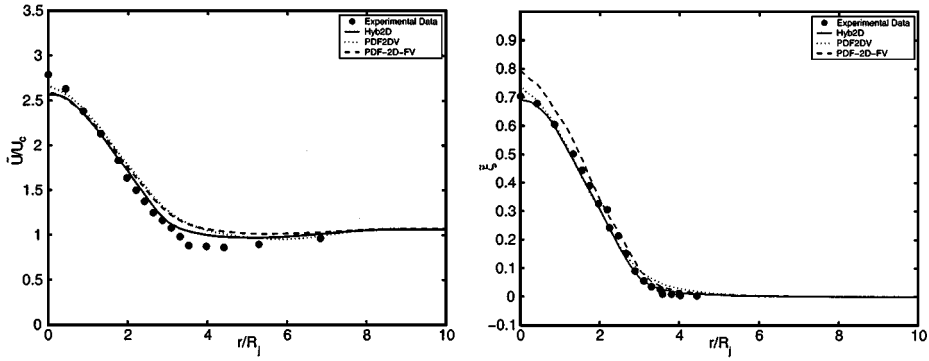

FIG. 3. Comparison of Favre-averaged mean axial velocity and mixture fraction at $x/R_j = 40$. Solid line: HYB2D (present); dashed line: PDF-2D-FV; dotted line: PDF2DV; symbols: Experimental data. Grid: 40×40, $N_{pc} = 80$, and $N_{TA} = 500$.

PDF-2D-FV. As can be seen in these figures, the present results are in good agreement with the other PDF simulations and also in remarkably good agreement with the experimental data considering the simple velocity, mixing, and chemistry models being used. Notice that the present result for the mean mixture fraction is in better agreement with the experimental data than results for the other PDF solution algorithms especially near the centerline. This is mainly due to the fact that the bias error is virtually eliminated in the present hybrid method as will be discussed in Section 6.4.

6.3. Statistical Stationarity

The HYB2D code is designed to treat only statistically stationary flows. To show the statistical stationarity of the numerical solutions, time series of Favre-averaged mean axial velocity and turbulent kinetic energy at four observation locations are depicted in Fig. 4. The results are obtained for a 48×48 grid with the number of particles per cell $N_{pc} = 40$. It can be seen that statistical stationarity is reached after about 5000 particle time steps. The initial fluctuations are mainly due to the relatively small time-averaging factor used in the early stages of the computation.

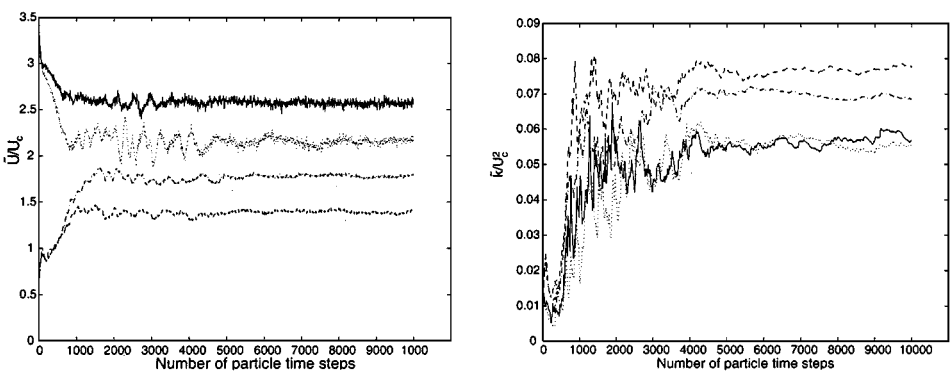

FIG. 4. Time histories of $\tilde{U}/U_c$ and of $\tilde{k}/U_c^2$ at locations $(x/R_j, r/R_j)$, (40, 0) (solid line), (72, 0) (dotted line), (40, 2.5) (dashed line), and (72, 2.5) (dashdot line), showing that statistically stationary state is achieved after about 5000 particle time steps.

6.4. Internal Consistency

In this section, the consistency conditions are investigated and the performance of the velocity, position, and energy correction algorithms is examined.

6.4.1. *Velocity Correction*

As discussed in Section 4.1, the consistency condition given by Eq. (56) (i.e., $\tilde{\mathbf{u}} = 0$) is enforced by the velocity correction algorithm. In all the results presented here, the velocity correction is performed at each particle time step but it is found that performing the correction once every two or three particle time steps is sufficient for this test case. The radial profiles of the time-averaged mean axial $\tilde{u}^P_{TA}$ and radial $\tilde{v}^P_{TA}$ fluctuating velocity components without and with the velocity correction applied are shown in Fig. 5 at the axial locations $x/R_j = 40$ and $x/R_j = 60$ to demonstrate the performance of the velocity correction algorithm. The figure clearly shows that, when the correction is turned off, the condition is not fully satisfied especially near the centerline but when the correction is turned on it is successfully enforced leaving only the statistical fluctuations.

6.4.2. *Position Correction*

The position correction is performed to enforce the consistency between q_{TA} and $\langle\rho\rangle_{TA}$ at the numerical solution level. As discussed in Section 4.2, the correction algorithm is

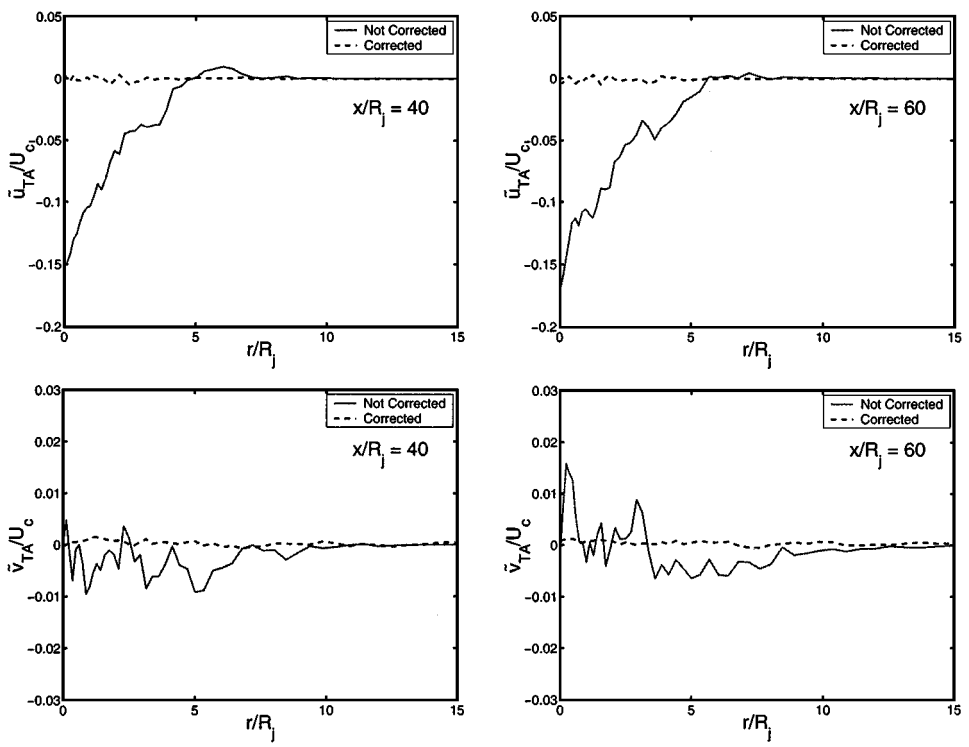

FIG. 5. Radial profiles of the time-averaged mean axial (upper plots) and radial (lower plots) fluctuating velocity components without the velocity correction (solid lines) and with the velocity correction (dashed lines) at $x/R_j = 40$ (left) and $x/R_j = 60$ (right). Grid: 48×48, $N_{pc} = 40$, and $N_{TA} = 500$.

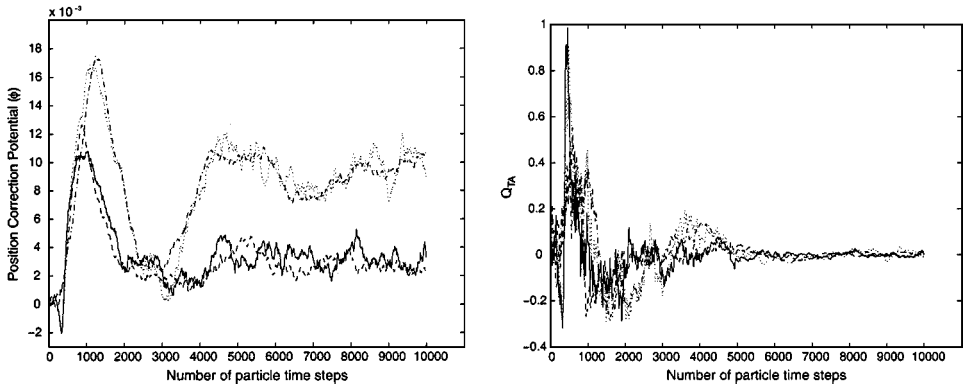

FIG. 6. Time histories of the position correction potential ϕ and of the time-averaged normalized density difference Q_{TA} at location $(x/R_j, r/R_j)$, (40, 0) (solid line), (72, 0) (dotted line), (40, 2.5) (dashed line), and (72, 2.5) (dashdot line). Grid: 48×48, $N_{pc} = 40$, and $N_{TA} = 500$.

designed such that the condition is satisfied exactly by relaxing the mean particle mass density smoothly to the particle mean density as a statistically stationary state is reached. All the results are obtained with the parameters $k_f = 3.0$, $k_b = 8.0$, $N_{TA}^c = 20$, $(CFL)_P = 0.4$, and $\epsilon_\zeta = 0.25$.

The time histories of the position correction potential ϕ and the time-averaged normalized density difference Q_{TA} are plotted in Fig. 6 to show the convergence of the algorithm. As can be seen from the comparison of this figure with the time histories of $\tilde{U}$ and $\tilde{k}$ plotted in Fig. 4, the position correction algorithm converges at about the same rate as the flow solver. Furthermore, it is clearly seen that Q_{TA} relaxes to zero as required when the statistically stationary state is reached.

The radial profiles of Q_{TA} without and with the position correction applied are shown in Fig. 7 at the axial locations $x/R_j = 5, 20, 40$, and 60 to demonstrate the effect of the correction algorithm. As can be seen in this figure, the consistency between q_{TA} and $\langle\rho\rangle_{TA}$ is not fully satisfied when the correction is turned off while it is successfully enforced by the correction algorithm everywhere in the computational domain leaving only the statistical fluctuations.

The position correction is effected through a correction velocity so that the magnitude of the correction velocity is a good measure for how much correction is performed. Figure 8 depicts the axial and radial correction velocity profiles at $x/R_j = 40$ evaluated at 500, 5000, and 10,000 particle time steps. It can be seen in this figure that the magnitudes of the axial and radial correction velocities are slightly larger in the transient regime and get smaller as a statistically stationary state is approached. In the statistically stationary state, the maximum magnitudes of the axial and radial correction velocities are about 8 and 10% of the coflow bulk velocity U_c, respectively.

6.4.3. *Energy Correction*

The energy correction is performed to relax the FV mean equivalent energy field to the corresponding particle field as discussed in Section 4.3.

As shown earlier, a value of f_e about unity is expected to lead to a smooth relaxation, and it is specified here as $f_e = 1.05$. The relaxation factor Ω_F has dimensions of a frequency

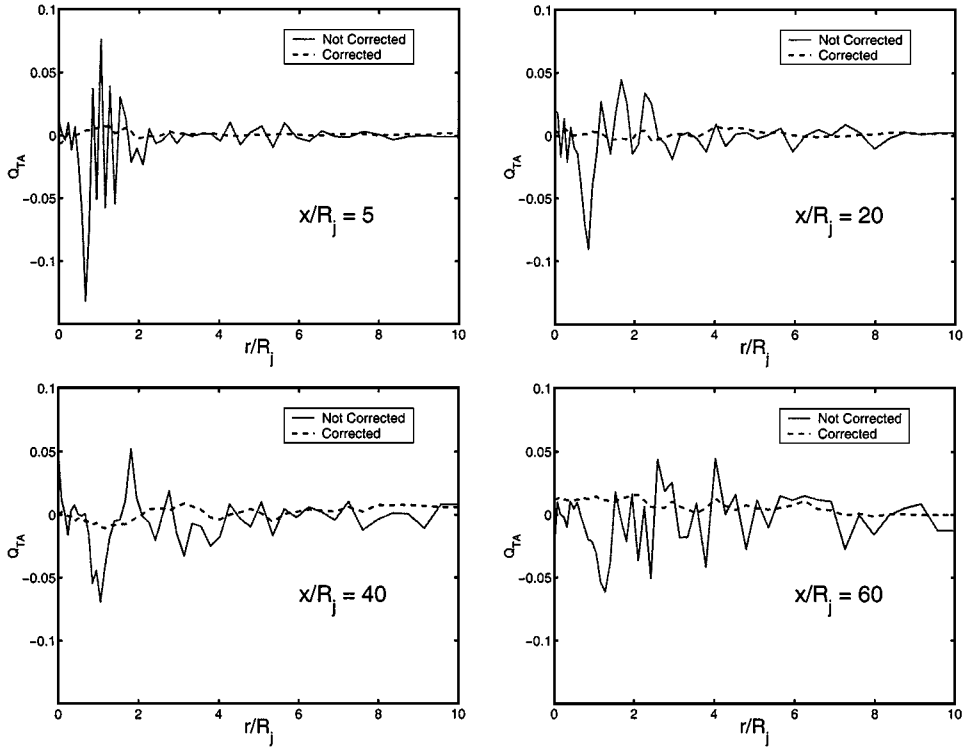

FIG. 7. Radial profiles of the time-averaged density difference Q_{TA} without the position correction (solid lines) and with the position correction (dashed lines) at $x/R_j = 5, 20, 40,$ and 60. Grid: 48×48, $N_{pc} = 40$, and $N_{TA} = 500$.

and is defined as

$$\Omega_F = f_{corr}/\tau_{corr}, \tag{91}$$

where τ_{corr} is a relaxation time scale chosen as the residence time based on the jet bulk velocity; i.e.,

$$\tau_{corr} = \frac{\mathcal{L}}{U_j}, \tag{92}$$

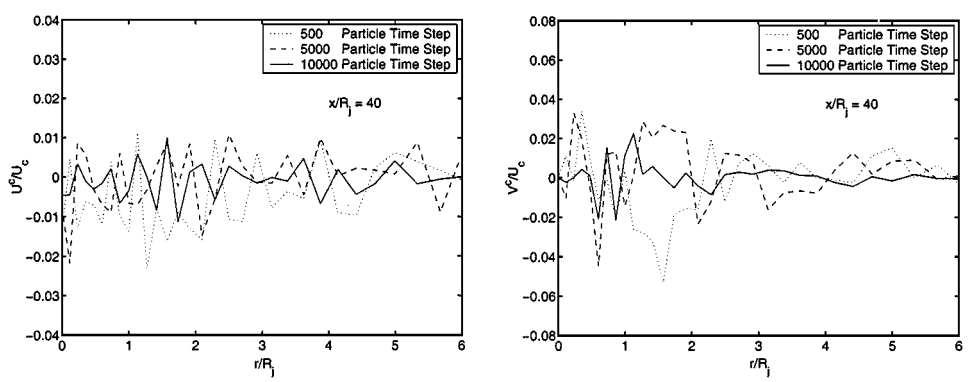

FIG. 8. The normalized axial (left plot) and radial (right plot) position correction velocity profiles evaluated at 500, 5000, and 10,000 particle time steps. Grid: 48×48, $N_{pc} = 40$, and $N_{TA} = 500$.

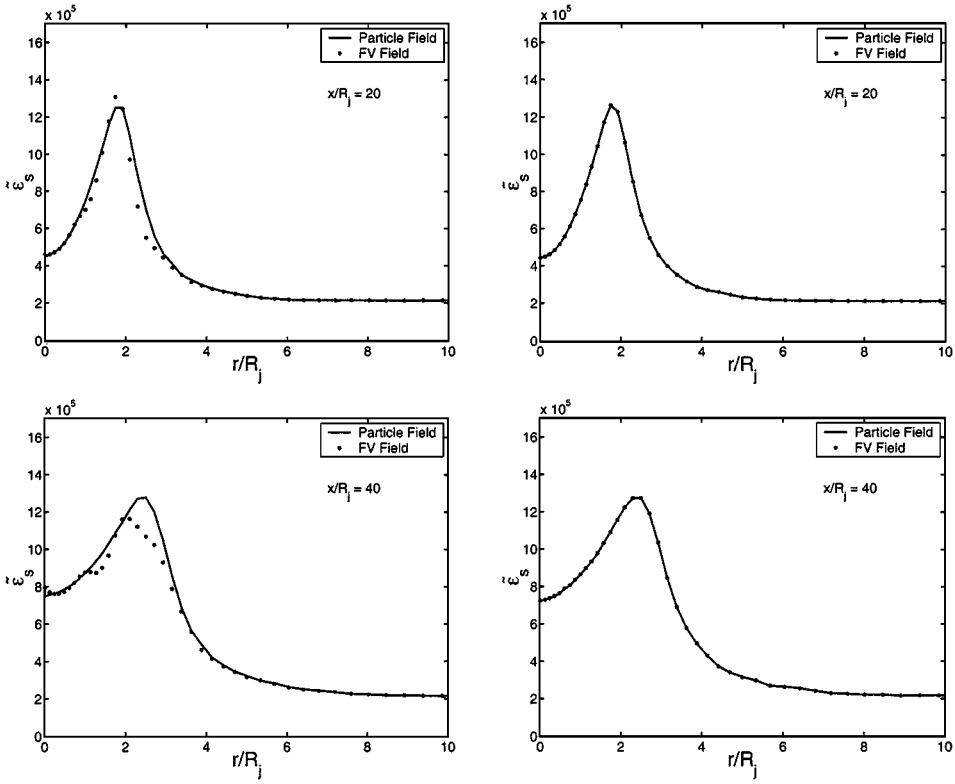

FIG. 9. Profiles of the mean FV and particle equivalent energy fields without the energy correction (left plots) and with the energy correction (right plots) at $x/R_j = 20$ (top plots) and at $R_j = 40$ (bottom plots). Grid: 48×48, $N_{pc} = 80$, and $N_{TA} = 500$.

where $\mathcal{L}$ is the length of the computational domain in the axial direction and U_j is the jet bulk velocity. The only remaining free parameter f_{corr} scales the relaxation time and it should be chosen as small as possible for a fast relaxation. On the other hand, too small values of f_{corr} may introduce an instability in the FV scheme. It is found that $f_{corr} = 1.0$ makes the FV sensible internal energy field relax smoothly to the corresponding particle field, but the results seem not very sensitive to the choice of f_{corr} in the range between $f_{corr} = 0.5$ and $f_{corr} = 5.0$.

The profiles of the FV and particle mean equivalent energy $\tilde{\epsilon}_s$ are plotted in Fig. 9 at two different axial locations without and with the correction being applied. For this test case, the full energy equation (Eq. (38)) is implemented so that it is consistent with the particle method (at the level of equations). The numerical simulations are performed on a 48×48 grid with the number of particles per cell $N_{pc} = 40$ and the final time-averaging factor $N_{TA} = 500$. These figures clearly show that consistency between the FV and particle mean energy fields is not achieved if the correction is not performed, but very good agreement between the two fields is recovered when the correction is applied.

In this hybrid method, the mean density is also represented by duplicate fields in the FV and particle methods, raising again a question of consistency. However, as shown in Section 3, consistency between the mean density fields is not independent and is guaranteed by the consistency of the mean energy fields. This is verified in Fig. 10. As can be seen in the figure, the agreement between FV and particle mean density fields is recovered

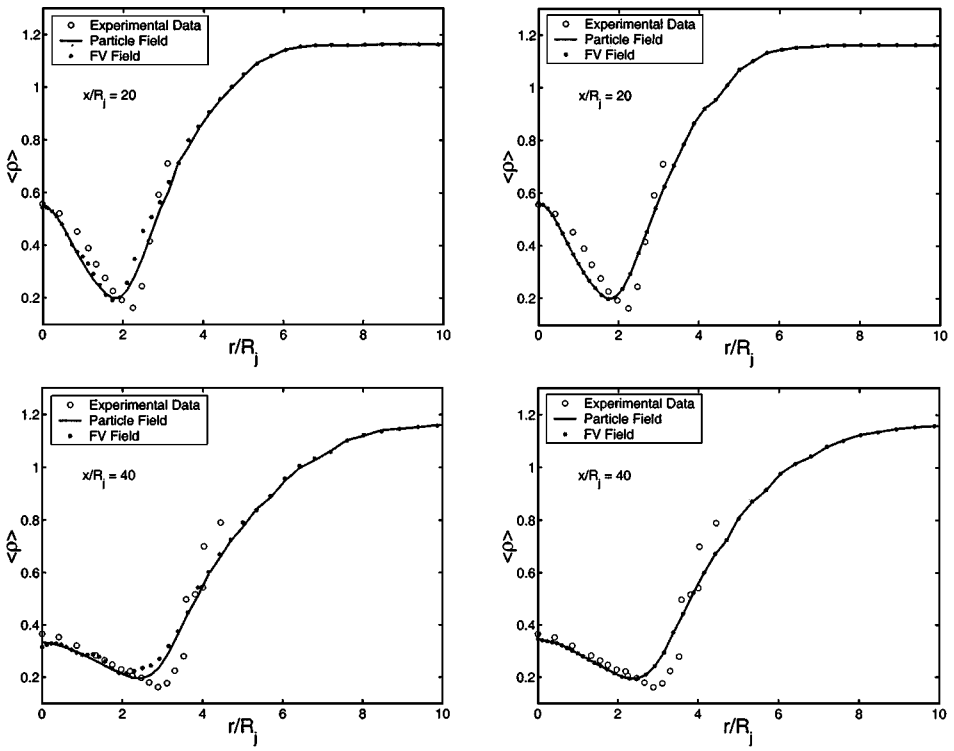

FIG. 10. Profiles of the mean FV and particle density fields without the energy correction (left plots) and with the energy correction (right plots) at $x/R_j = 20$ (top plots) and at $R_j = 40$ (bottom plots). Grid: 48×48, $N_{pc} = 80$, and $N_{TA} = 500$.

consistently as the FV energy field is relaxed to the the corresponding particle field by the energy correction algorithm.

6.5. Spatial Discretization Error

Spatial discretization error results from the spatial discretization in the FV method and also from the kernel estimation and interpolation schemes in the particle algorithm due to the finite size of the mesh cells. The spatial error in the present hybrid method has been previously examined extensively by Muradoglu *et al.* [12] and it has been shown that the method is second-order accurate in space. Therefore, an extensive study of spatial discretization error is not repeated here but results intended to show grid convergence are presented. For this purpose, the time-averaged profiles of mean axial velocity, mean turbulent kinetic energy, mean turbulent frequency, and mean mixture fraction are plotted in Fig. 11 at the axial location $x/R_j = 40$ for successively refined grids. In these figures, the profiles obtained by Richardson extrapolation assuming second-order accuracy in space and using 48×48 and 64×64 grids are also plotted. All the simulations are performed with the number of particles per cell $N_{pc} = 40$ and the time-averaging factor $N_{TA} = 500$. It is clearly seen in these figures that the difference among the profiles is decreasing with cell refinement, indicating that grid convergence is achieved. To verify the second-order spatial accuracy of the method, the mean quantities, $\tilde{U}/U_c$, $\tilde{k}/U_c^2$, $\tilde{\omega}R_j/U_j$, and $\tilde{\xi}$ are also plotted against M^{-2} at the location $(x/R_j, r/R_j) = (40, 1)$ in Fig. 12 in which the symbols

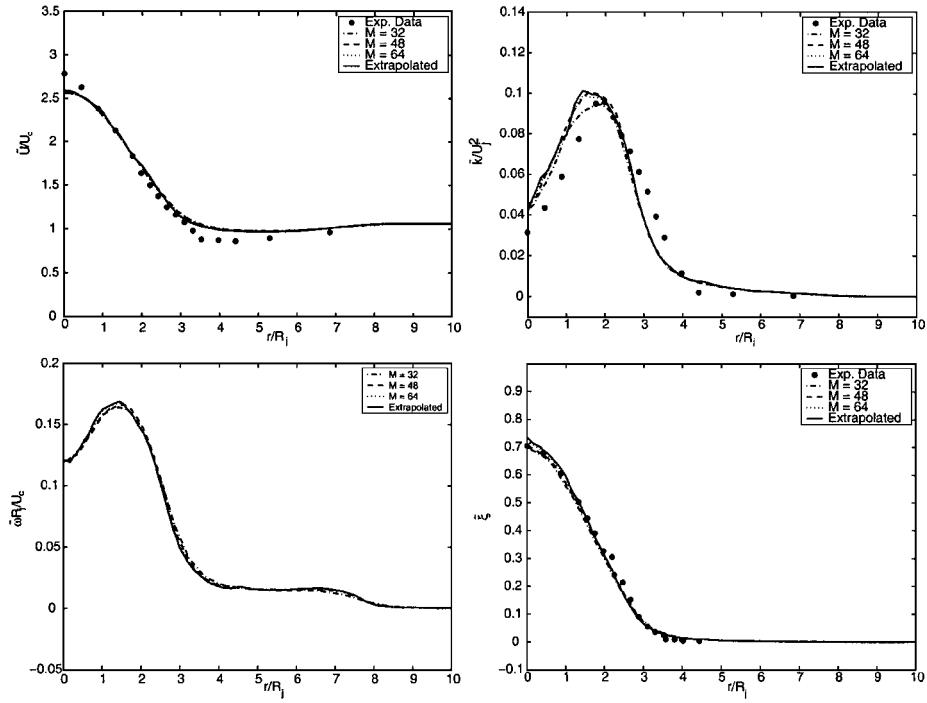

FIG. 11. Time-averaged mean profiles at $x/R_j = 40$ with $N_{pc} = 80$ and $N_{TA} = 500$ on various grids ranging between $M = 32$ and $M = 64$. The solid lines represent the values obtained by Richardson extrapolation assuming second-order spatial accuracy and using the solutions with $M = 48$ and $M = 64$.

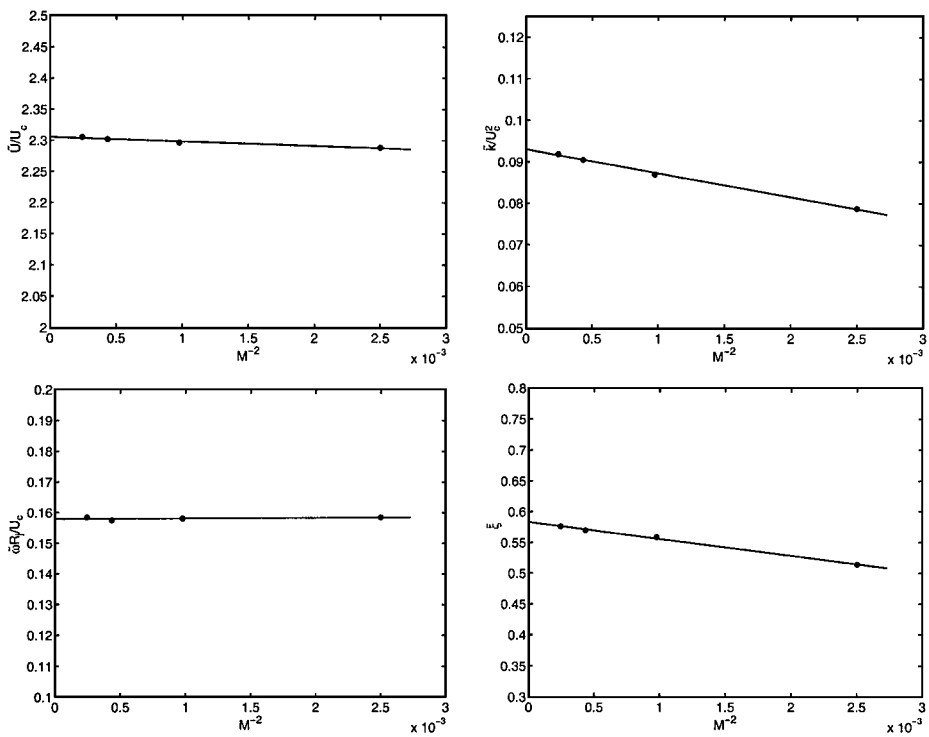

FIG. 12. Time-averaged mean quantities against M^{-2} at $(x/R_j, r/R_j) = (40.0, 1.0)$ showing the exepected second-order spatial accuracy of the method. Solid lines are linear least-squares fits to data.

represent the numerical data and the solid lines are the linear least-squares fits to the data. As can be seen in the figure, the approximate linear relationship between the mean quantities and M^{-2} confirms the expected second-order spatial accuracy of the method. We also note that the 36×36 grid (corresponding to $M^{-2} = 0.77 \times 10^{-3}$) is sufficient for the spatial error to be less than 5% in all the mean quantities at this location.

6.6. Bias Error

Bias error is the deterministic error caused by using a finite number of particles. Simulations with a 48×48 grid but with various numbers of particles per cell are performed to explore the bias error in various mean quantities. The bias error is expected to scale as N_{pc}^{-1} [18, 12]. Figure 13 shows the values of the normalized mean quantities, $\tilde{U}/U_c$, $\tilde{k}/U_c^2$, $\tilde{\xi}$, and $\tilde{\omega}R_j/U_j$ with N_{pc}^{-1} at the observation point $(x/R_j, r/R_j) = (40.0, 1.0)$. The symbols represent the values obtained for $N_{pc} = 20$, 40, 80, and 160 and the solid lines are the linear least-squares fits to the data points. The approximate linear relationship between the mean quantities and N_{pc}^{-1} confirms the expected scaling of the bias error. The slopes of the lines indicate the sensitivity of the solutions to bias error. It is clearly seen that the bias error for a given value of N_{pc} in the present hybrid method is much smaller than in the stand-alone particle/mesh method, and still smaller than (but comparable to) the bias in the tightly coupled hybrid algorithm. For example, to obtain a solution with the bias error less than 5% in all the mean quantities at the location $(x/R_j, r/R_j) = (40, 1)$, the present

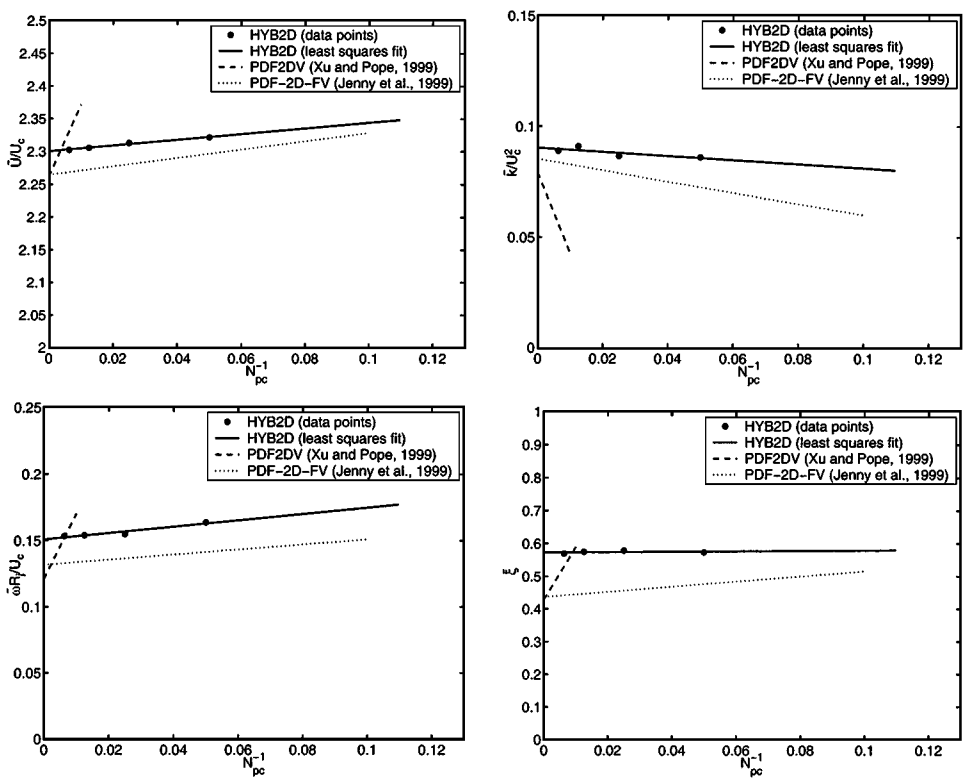

FIG. 13. Time-averaged mean quantities against N_{pc}^{-1} at $(x/R_j, r/R_j) = (40.0, 1.0)$. Symbols: HYB2D (data points); solid lines: HYB2D (linear least squares); dotted lines: PDF2DV; dashed lines: PDF-2D-FV.

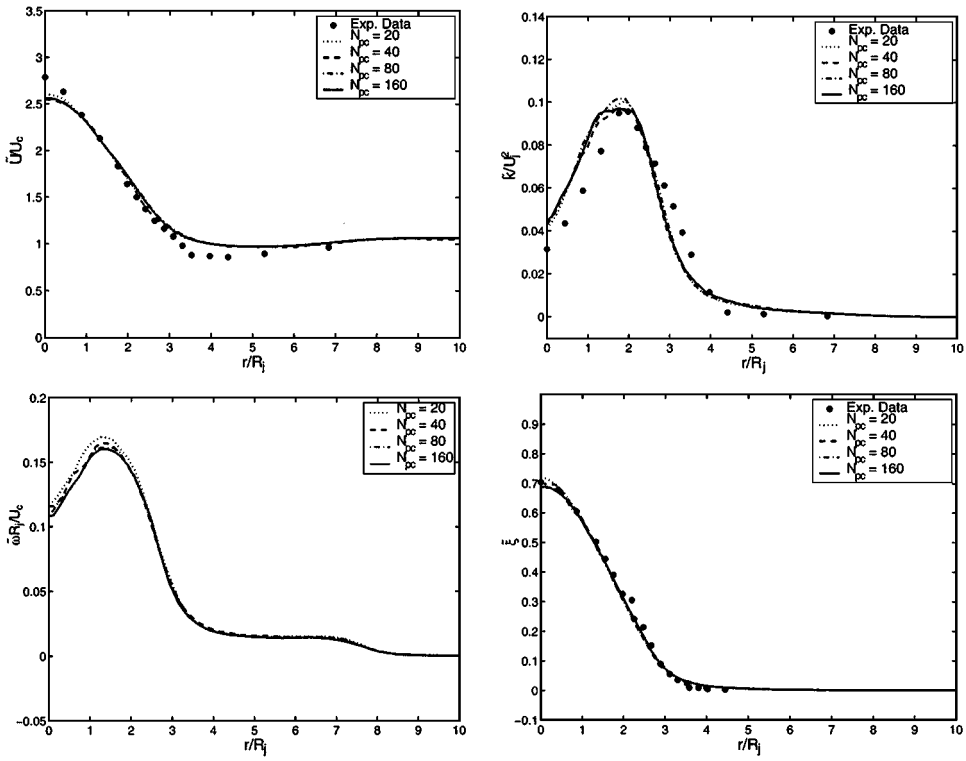

FIG. 14. Time-averaged mean profiles at $x/R_j = 40$ with $M = 48$ and N_{pc} range from 20 to 160, showing the overall variations of the bias error in the mean quantities $\tilde{U}/U_c$, $\tilde{k}/U_c^2$, $\tilde{\omega}R_j/U_c$, and $\tilde{\xi}$.

hybrid method requires only about 20 particles per cell while the stand-alone particle/mesh method PDF2DV and the tightly coupled consistent hybrid method PDF-2D-FV require about 920 and 60 particles per cell, respectively.

The normalized profiles of mean axial velocity, mean turbulent kinetic energy, mean turbulence frequency, and mean mixture fraction are plotted in Fig. 14 at $x/R_j = 40$ for $N_{pc} = 20$, 40, 80, 160 to show the overall variations of the bias errors in these quantities. It is seen that differences between profiles of all the quantities are quite small, indicating that the bias error is virtually eliminated in the present hybrid algorithm.

A different position correction algorithm, referred to here as the "old position correction algorithm" is used in the PDF2DV code [17]. The old position correction algorithm is designed to enforce the consistency between the geometric volume and the particle volume as expressed by Eq. (51). In this approach, particle positions are corrected to satisfy the condition (to within a given error tolerance) at each particle time step, which results in excessive jittering in the particle positions leading to large bias error.

To explore the reduction in the bias error by the present position correction algorithm, the old position correction algorithm is also implemented in the present hybrid code HYB2D. The normalized mean quantities $\tilde{U}/U_c$, $\tilde{k}/U_c^2$, $\tilde{\xi}$ and $\tilde{\omega}R_j/U_c$ obtained with the old and new position correction algorithms are plotted in Fig. 15 against N_{pc}^{-1} at $(x/R_j, r/R_j) = (40, 0)$. It is clearly seen that the present correction algorithm results in much smaller bias error than the old algorithm especially in the turbulent kinetic energy and the mean mixture fraction. For instance, to obtain a solution with the bias error less than 5% in all the mean quantities at

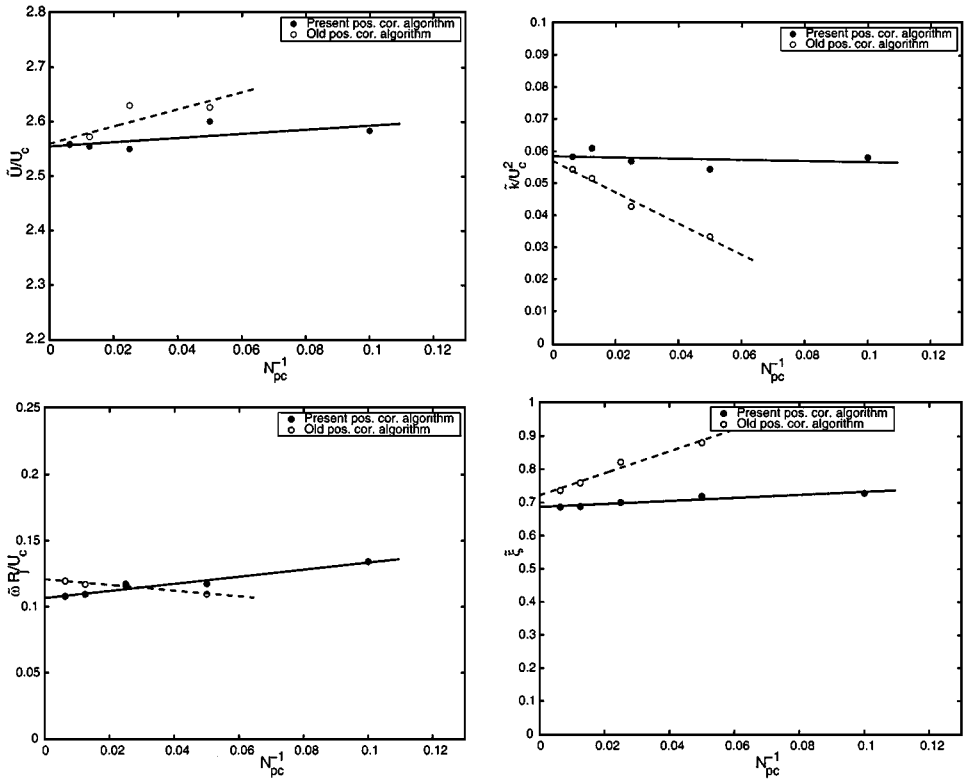

FIG. 15. Time-averaged mean quantities against N_{pc}^{-1} at $(x/R_j, r/R_j) = (40.0, 0.0)$, showing the reduction in the bias error by the present position correction algorithm. Grid: 48×48 and $N_{pc} \times N_{TA} = 20{,}000$. The symbols are the numerical data and the lines are the linear least-squares fits to the data.

the location $(x/R_j, r/R_j) = (40, 0)$, the present hybrid method requires about 20 particles per cell with the present position correction algorithm while it requires about 170 particles per cell with the old position correction algorithm.

7. CONCLUSIONS

The consistent hybrid algorithm implemented in the HYB2D code is developed to solve the modeled transport equation for the joint PDF of velocity, turbulence frequency, and compositions for turbulent reactive flows, and it is applied to a reacting piloted-jet flame (Flame-L). It is shown that the method is convergent and the bias and spatial errors converge at the expected rates. The results are compared and found to be in good agreement with the experimental data and with the results of earlier PDF simulations of Xu and Pope [23] and Jenny *et al.* [7].

The present hybrid method is shown to be completely consistent at the level of the governing equations and its full consistency at the numerical solution level is carefully examined. Three conditions given by Eqs. (53), (56), and (57) are identified as the independent consistency conditions and shown to be necessary and sufficient conditions to be fulfilled for the full consistency at the numerical solution level, correcting the earlier paper by Muradoglu *et al.* [12], where only two of these conditions, i.e., those given by Eqs. (56) and (57), were mistakingly claimed to be sufficient conditions for full consistency.

The independent consistency conditions are enforced by the use of velocity, position, and energy correction algorithms to make the method fully consistent at the numerical level. The velocity correction algorithm (Eq. (63)) is devised to correct the particle fluctuating velocity to enforce the condition given by Eq. (53). It is found that the algorithm is very robust and performs well. The main advantage of the velocity correction algorithm is that it is very simple to implement and requires very little additional computational work.

The position correction algorithm (Eqs. (66)–(69)) corrects the particle position to enforce the condition given by Eq. (56) by relaxing the mean particle mass density q to the particle mean density $\langle\rho\rangle$ as a statistically stationary state is reached. An analysis is performed to determine an approximately optimal set of the parameters used in the position correction algorithm in order to attain the statistically stationary sate quickly and with small fluctuations. Even though the analysis is based on the modified version of the algorithm and carried out only for a constant-density flow, it is found that the algorithm with this set of parameters is very robust and performs very well for the test case studied here.

The final independent consistency condition (Eq. (57)) is enforced by the use of the energy correction algorithm given by Eqs. (86) and (87). The energy correction algorithm is performed in the FV algorithm and used to relax the FV mean energy field $\tilde{\epsilon}_s^{FV}$ to its particle counterpart. The algorithm is analyzed based on a mass-spring-damper system and the correction parameters are determined to achieve a smooth relaxation. It is found that the algorithm is very robust to small variations in the parameters and performs very well. It is emphasized here that the use of the energy correction algorithm greatly improves the robustness of the FV algorithm since it allows the removal of some noisy particle fields (such as the scalar fluxes) from the mean energy conservation equation.

A simple formulation is developed for the implementation of the general ideal gas equation of state, which keeps the ratio of specific heats constant and greatly simplifies the mean conservation equations for the implementation of the FV algorithm.

It is found that the present hybrid method is very effective at virtually eliminating the bias error in all the mean quantities. It is also found that the new position correction algorithm substantially reduces the bias error especially in the turbulent kinetic energy and the mean mixture fraction compared to the alternative correction algorithm implemented in PDF2DV [17] code. For a given grid size and number of particles, the numerical errors in the present hybrid method are substantially less than in other methods—by a factor of 46 compared to the much-used, stand-alone particle/mesh method implemented in PDF2DV [17]. Hence the present method represents a substantial advance in computational efficiency.

While the present work is in the context of the velocity–frequency–compositions joint PDF, most of the methodology developed is applicable to the compositions PDF; specifically the position and energy correction algorithms, and the treatment of the equation of state. The present hybrid method can be readily applied to the 3D flows and to different grids (e.g., unstructured grids). However, because it relies on statistical stationarity and time-averaging, it cannot be extended straightforwardly to unsteady flows.

8. APPENDIX:

The position correction algorithm presented in Section 4.2 is shown to guarantee the consistency between the mean particle mass density and the particle mean density in a time-averaged sense if a statistically stationary state is reached. Here the algorithm is analyzed

to address the the question of the statistical stationarity, and the parameters are optimized to attain the statistically stationary state quickly and with small fluctuations.

The algorithm given by Eqs. (65)–(69) are slightly modified to facilitate a simple analysis of the algorithm. The modified algorithm is then given by

$$qU_i^c = -\frac{\partial \phi}{\partial x_i} - aU_o L\left[\zeta \frac{\partial \bar{Q}}{\partial x_i} + (1-\zeta)\frac{\partial Q}{\partial x_i}\right] \tag{93}$$

$$\frac{\partial \phi}{\partial t} = bU_o^2 Q \tag{94}$$

$$\frac{\partial \bar{Q}}{\partial t} = -(\bar{Q} - Q)c\frac{U_o}{L} + fU_o L\frac{\partial^2 \bar{Q}}{\partial x_i \partial x_i} \tag{95}$$

$$Q = q - \langle \rho \rangle \tag{96}$$

$$\zeta = \begin{cases} 1 & \text{if } \frac{\langle q \rangle}{\langle \rho \rangle} \geq \epsilon_\zeta \\ 0 & \text{if } \frac{\langle q \rangle}{\langle \rho \rangle} < \epsilon_\zeta. \end{cases} \tag{97}$$

To analyze the algorithm, we consider a constant-density incompressible flow and assume that the Favre-averaged mean velocity field $\tilde{\mathbf{U}}$ is steady. With these assumptions, the mean continuity equations based on $\langle \rho \rangle$ and q can be given by [14]

$$\frac{\partial \langle \rho \rangle}{\partial t} + \frac{\partial}{\partial x_i}(\langle \rho \rangle \tilde{U}_i) = 0 \tag{98}$$

and

$$\frac{\partial q}{\partial t} + \frac{\partial}{\partial x_i}\left(q\tilde{U}_i + qU_i^c\right) = 0. \tag{99}$$

Subtracting Eq. (98) from Eq. (99) yields

$$\frac{\partial Q}{\partial t} + \frac{\partial}{\partial x_i}\left(Q\tilde{U}_i + qU_i^c\right) = 0. \tag{100}$$

Considering the case $\zeta = 1$ first and substituting Eq. (93) into Eq. (100) then results in

$$\frac{\partial Q}{\partial t} + \frac{\partial}{\partial x_i}(Q\tilde{U}_i) - \frac{\partial^2 \phi}{\partial x_i \partial x_i} - aU_o L\frac{\partial^2 \bar{Q}}{\partial x_i \partial x_i} = 0. \tag{101}$$

From Eq. (95), we have

$$Q = \frac{L}{U_o c}\frac{\partial \bar{Q}}{\partial t} + \bar{Q} - \frac{fL^2}{c}\frac{\partial^2 \bar{Q}}{\partial x_i \partial x_i}, \tag{102}$$

which can be substituted into Eq. (101) to give

$$\frac{L}{U_o c}\frac{\partial^2 \bar{Q}}{\partial t^2} + \frac{\partial \bar{Q}}{\partial t} - \frac{fL^2}{c}\frac{\partial^2}{\partial x_i \partial x_i}\left(\frac{\partial \bar{Q}}{\partial t}\right) - \frac{\partial^2 \phi}{\partial x_i \partial x_i} - aU_o L\frac{\partial^2 \bar{Q}}{\partial x_i \partial x_i} + \tilde{U}_i\frac{\partial}{\partial x_i}\left[\frac{L}{U_o c}\frac{\partial \bar{Q}}{\partial t} + \bar{Q} - \frac{fL^2}{c}\frac{\partial^2 \bar{Q}}{\partial x_j \partial x_j}\right] = 0, \tag{103}$$

where the constant-density assumption, i.e., $\frac{\partial \tilde{U}_i}{\partial x_i} = 0$, has been used. Diffierentiating Eq. (102) with respect to time and using Eqs. (94) and (102) yields

$$\frac{\partial^3 \bar{Q}}{\partial \hat{t}^3} + \frac{\partial^2 \bar{Q}}{\partial \hat{t}^2} - \frac{fL^2}{c}\frac{\partial^2}{\partial x_i \partial x_i}\left(\frac{\partial^2 \bar{Q}}{\partial \hat{t}^2}\right) - \frac{aL^2}{c}\frac{\partial^2}{\partial x_i \partial x_i}\left(\frac{\partial \bar{Q}}{\partial \hat{t}}\right) - \frac{bL^2}{c^2}\frac{\partial^2}{\partial x_i \partial x_i}\left[\frac{\partial \bar{Q}}{\partial \hat{t}} + \bar{Q} - \frac{fL^2}{c}\frac{\partial^2 \bar{Q}}{\partial x_j \partial x_j}\right] + \frac{L}{U_o c}\tilde{U}_i \frac{\partial}{\partial x_i}\left[\frac{\partial^2 \bar{Q}}{\partial \hat{t}^2} + \frac{\partial \bar{Q}}{\partial \hat{t}} - \frac{fL^2}{c}\frac{\partial^2}{\partial x_j \partial x_j}\left(\frac{\partial \bar{Q}}{\partial \hat{t}}\right)\right] = 0, \tag{104}$$

where the non-dimensional time variable $\hat{t}$ is defined as

$$\hat{t} \equiv \frac{U_o c}{L} t. \tag{105}$$

With an assumption of periodic boundary conditions, the spatial Fourier transform of Eq. (103) is given by

$$\frac{\partial^3 \hat{\bar{Q}}}{\partial \hat{t}^3} + \left[1 + \frac{f}{c}(\kappa^2 L^2) + \sigma i\right]\frac{\partial^2 \hat{\bar{Q}}}{\partial \hat{t}} + \left[\left(\frac{a}{c} + \frac{b}{c^2}\right)(\kappa^2 L^2) + \left(1 + \frac{f}{c}(\kappa^2 L^2)\right)\sigma i\right]\frac{\partial \hat{\bar{Q}}}{\partial \hat{t}} + \frac{b}{c^2}\left[1 + \frac{f}{c}(\kappa^2 L^2)\right](\kappa^2 L^2)\hat{\bar{Q}} = 0, \tag{106}$$

where $\hat{\bar{Q}}$ is the Fourier transform of $\bar{Q}$, κ is the wave number vector, and $i = \sqrt{-1}$. The scalar κ and the non-dimensional parameter σ are defined as

$$\kappa = \sqrt{\kappa_i \kappa_i}, \tag{107}$$

and

$$\sigma = \frac{L}{U_o c}(\tilde{U}_i \kappa_i). \tag{108}$$

Now let the length scale L be specified as

$$L = \kappa_{\max}^{-1}, \tag{109}$$

where $\kappa_{\max}$ is the maximum wavenumber (on the grid to be specified) and define

$$k = (\kappa/\kappa_{\max})^2 = \kappa^2 L^2 \leq 1. \tag{110}$$

Then looking for a solution in the form

$$\hat{\bar{Q}} = \hat{\bar{Q}}_o e^{\hat{\alpha}\hat{t}}, \tag{111}$$

where $\hat{\bar{Q}}_o$ is a function of space only, and substituting Eq. (111) into Eq. (105) yields the following characteristic equation for $\hat{\alpha}$

$$\hat{\alpha}^3 + \left(1 + k\frac{f}{c} + \sigma i\right)\hat{\alpha}^2 + \left[k\left(\frac{a}{c} + \frac{b}{c^2}\right) + \left(1 + k\frac{f}{c}\right)\sigma i\right]\hat{\alpha} + k\frac{b}{c^2}\left(1 + k\frac{f}{c}\right) = 0. \tag{112}$$

Note that the real parts of all the roots of Eq. (112) must be strictly negative and as small as possible for good damping and convergence of the algorithm. The maximum of the real parts of the characteristic equation determines the rate of convergence of the correction algorithm, so this quantity is referred to as the "damping factor." For the sake of simplicity, we consider a uniform grid so that the maximum wavenumber is given by

$$L^{-1} = \kappa_{\max} = \frac{\pi}{\Delta x}, \tag{113}$$

where Δx is the grid spacing. Hence the time-averaging time scale is

$$\tau_{TA}^{c} \equiv \frac{L}{U_o c} = \frac{\Delta x}{\pi U_o c}. \tag{114}$$

The time-averaging time scale is typically specified in terms of a number of particle time steps; i.e.,

$$\tau_{TA}^{c} = N_{TA}^{c} \Delta t, \tag{115}$$

where Δt is the time step taken in the particle algorithm and N_{TA}^{c} is a free parameter to be specified. From Eqs. (114) and (115), we get

$$c = \frac{1}{\pi N_{TA}^{c}} \frac{\Delta x}{U_o \Delta t}. \tag{116}$$

In the particle algorithm, the time step is determined according to a CFL condition defined as

$$(CFL)_P = \frac{|U|_{\max} \Delta t}{\Delta x}. \tag{117}$$

If we let U_o be specified as

$$U_o = |U|_{\max}, \tag{118}$$

and then the parameter c is obtained from Eqs. (116)–(118) as

$$c = \frac{1}{\pi} \frac{1}{(CFL)_P N_{TA}^{c}}. \tag{119}$$

To determine the other coefficients, we first consider the special case of zero mean convective velocity; i.e., $\tilde{\mathbf{U}} \equiv 0$ so that $\sigma \equiv 0$ for the maximum wavenumber, $k = 1$, in which case Eq. (112) reduces to

$$\hat{\alpha}^3 + \left(1 + \frac{f}{c}\right) \hat{\alpha}^2 + \left(\frac{a}{c} + \frac{b}{c^2}\right) \hat{\alpha} + \frac{b}{c^2} \left(1 + \frac{f}{c}\right) = 0. \tag{120}$$

Since it is difficult to solve Eq. (120) explicitly, we pose it as an inverse problem and require the first root be given by

$$\hat{\alpha}_1 = -1, \tag{121}$$

for which we must have

$$a = f \left(1 + \frac{b}{c^2}\right). \tag{122}$$

Using Eq. (122), Eq. (120) can be factored as

$$(\hat{\alpha}+1)\left(\hat{\alpha}^2+\frac{f}{c}\hat{\alpha}+\frac{b}{c^2}\left(1+\frac{f}{c}\right)\right)=0, \tag{123}$$

which can be solved to give

$$\hat{\alpha}_{2,3}=\frac{f}{c}\left(-1\pm\sqrt{1-4\frac{b}{f^2}\left(1+\frac{f}{c}\right)}\right). \tag{124}$$

If we choose

$$f=k_f c \tag{125}$$

$$b=k_b f^2, \tag{126}$$

where $k_f \geq 0$ and $k_b \geq 0$ are positive real numbers to be specified and require $4k_b(1+k_f)>1$, the real parts of the roots are given by

$$\text{Real}(\hat{\alpha})=\{-1,-k_f,-k_f\} \tag{127}$$

showing that the algorithm has good damping characteristics for this special case.

For the general case, Eq. (112) can be solved numerically over a range of convective velocities and wavenumbers. Figure 16 shows a surface plot of the damping factor for the parameters $k_f=3.0$, $k_b=8.0$, and $N_{TA}^c=20$. The figure clearly demonstrates that the

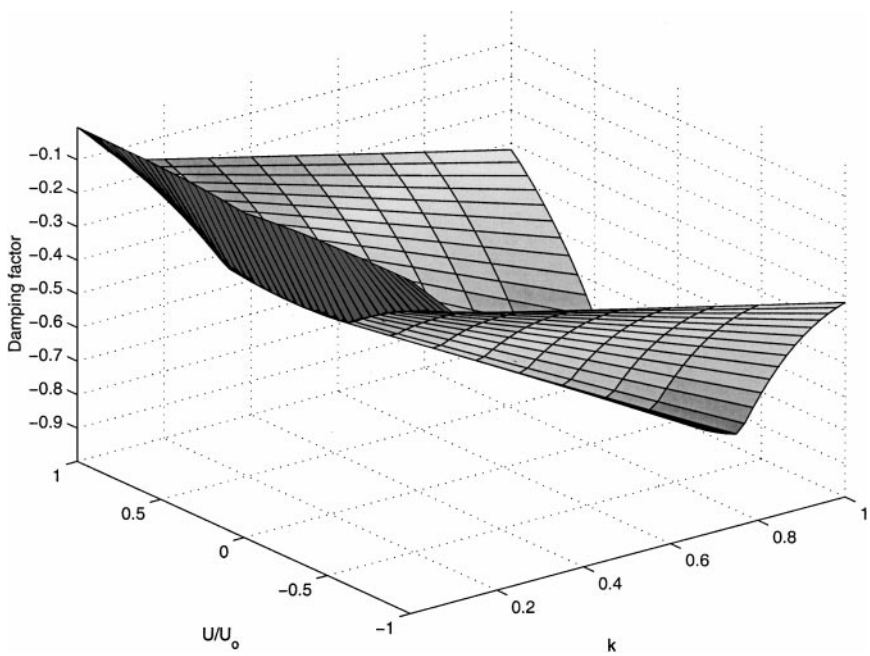

FIG. 16. The surface plot of the damping factor over the full ranges of the wavenumbers and convective velocity for $\zeta=1$.

damping factor is strictly negative and the algorithm has good damping characteristics for high wavenumbers and smaller mean convective velocity, but the damping gets worse as the wavenumber decreases and the convective velocity increases.

Time-averaging introduces a time scale which prevents the correction algorithm from responding quickly to the inconsistencies if the correction velocity is based purely on the time-averaged quantities such as ϕ and $\bar{Q}$. This may cause a numerical difficulty of having too many "empty cells" (i.e., cells devoid of particles), especially in a transient regime when a small number of particles per cell is used in a simulation. Therefore we consider replacing $\bar{Q}$ in Eq. (93) with its instantaneous counterpart Q, which corresponds to the case $\zeta = 0$. Following the same procedure as described above for the case $\zeta = 1$, the characteristic equation for the case $\zeta = 0$ can be seen to be

$$\hat{\alpha}^2 + \left(k\frac{a}{c} + \sigma i\right)\hat{\alpha} + k\frac{b}{c^2} = 0, \tag{128}$$

which can be solved to give

$$\hat{\alpha}_{1,2} = -k\frac{a}{2c} - \sigma i \pm \frac{1}{2}\sqrt{\left(k\frac{a}{c} + \sigma i\right)^2 - 4k\frac{b}{c^2}}. \tag{129}$$

Notice that both roots are real and strictly negative in the absence of the convective velocity; i.e., $\sigma = 0$. In general, the roots are complex and the damping factor for this case is plotted in Fig. 17, which indicates very good damping characteristics over wide ranges of wavenumbers and convective velocities.

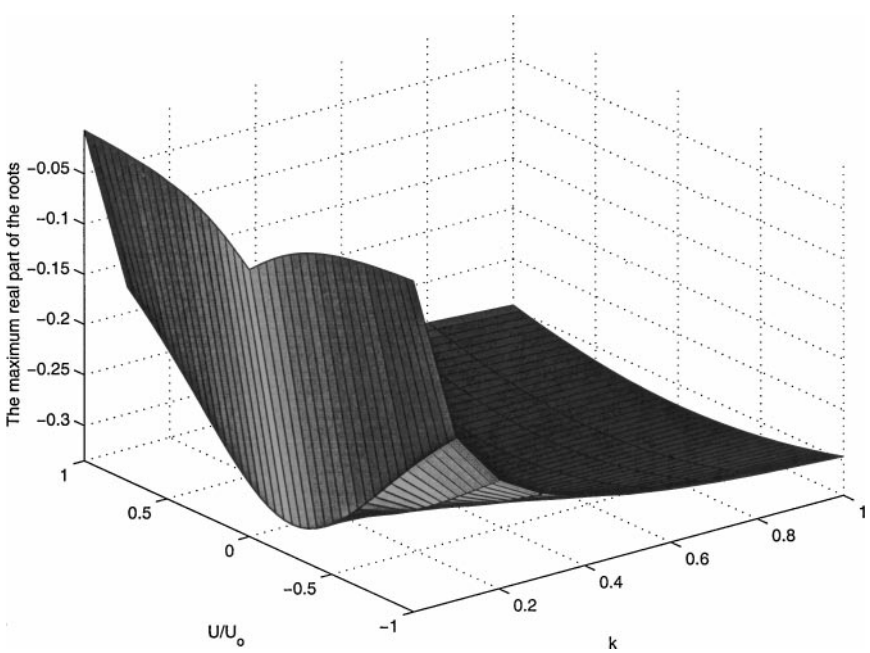

FIG. 17. The surface plot of the damping factor over the full ranges of the wavenumbers and convective velocity for the case $\zeta = 0$.

In spite of the fact that the case $\zeta = 0$ has a better damping characteristic than the case $\zeta = 1$, the case $\zeta = 0$ is not desirable since the use of the instantaneous particle field in Eq. (93) results in too much statistical noise in the correction velocity, especially when a small number of particles per cell is used. In addition to this, the instantaneous particle mass density used in Eqs. (93) is also a large source of statistical noise in the correction velocity. To avoid these deficiencies as much as possible, the best features of the both cases are combined and the final form of the position correction algorithm is given by Eqs. (65)–(69).

ACKNOWLEDGMENTS

This work is supported in part by Department of Energy, Grant DE-FG02-90ER 14128. The authors thank Dr. Patrick Jenny for the useful discussions in the early stages of developing the position correction algorithm.

REFERENCES

1. D. A. Caughey, Diagonal implicit multigrid algorithm for the Euler equations, *AIAA J.* **26**, 841(1988).
2. G.-C. Chang, *A Monte Carlo PDF/Finite-Volume Study of turbulent Flame*, Ph.D. thesis (Cornell University, 1996).
3. S. M. Correa and S. B. Pope, Comparision of a Monte Carlo, PDF finite-volume mean flow model with bluff-body Raman data, in *Twenty-Fourth Symp. International, on Combust., Pittsburgh, 1992* (The Combustion Institute), P. 279.
4. C. Dopazo, Recent development in PDF methods, in *Turbulent Reacting Flows*, edited by P. A. Libby and F. A. Williams (Academic Press, London, 1994), Chap. 7, p. 375.
5. T. D. Dreeben and S. B. Pope, *Nonparametric Estimation of Mean Fields with Application to Particle Methods for Turbulent Flows*, Technical Report FDA 92-13 (Cornell University, Ithaca, NY, 1992).
6. R. W. Hockney and J. W. Eastwood, *Computer Simulations Using Particles* (Hilger, Bristol, 1988).
7. P. Jenny, S. B. Pope, M. Muradoglu, and D. A. Caughey, A hybrid algorithm for the joint PDF equation of turbulent reactive flows, *J. Comput. Phys.* **166**, 218 (2001), doi:10.1006/jcph.2000.6646.
8. P. Jenny, M. Muradoglu, S. B. Pope, and D. A. Caughey, PDF simulations of a bluff-body stabilized flow, *J. Comput. Phys.* **169**, 1 (2001), doi:10.1006/jcph.2001.6704.
9. A. R. Masri, *Energy and Environmental Research*, Technical report (The University of Sydney, Sydney, Australia); avaliable at http://www.mech.eng.usyd.edu.au/research/energy/.
10. A. R. Masri, R. W. Dibble, and R. S. Barlow, The structure of turbulent nonpremixed flames revealed by Raman–Rayleigh–LIF measurements, *Prog. Energy Combust. Sci.* **22**, 307 (1996).
11. A. R. Masri and R. W. Bilger, Turbulent non-premixed flames of hydrocarbon fuels near extinction: Mean structure from probe measurements, in *Twenty-First Symp. (International) on Combust., Pittsburgh, 1988* (The Combustion Institute).
12. M. Muradoglu, S. B. Pope, P. Jenny, and D. A. Caughey. A consistent hybrid finite-volume/particle method for the PDF equations of turbulent reactive flows, *J. Comput. Phys.* **154**, 342 (1999).
13. S. B. Pope, A Monte Carlo method for the PDF equations of turbulent reactive flow, *Combust. Sci. Technol.* **25**, 159 (1981).
14. S. B. Pope, PDF methods for turbulent reactive flows, *Prog. Energy. Combust. Sci.* **11**, 119 (1985).
15. S. B. Pope, Lagrangian PDF methods for turbulent flows, *Annu. Rev. Fluid. Mech.* **26**, 23 (1994).
16. S. B. Pope, On the relationship between stochastic Lagrangian models of turbulence and second-moment closures, *Phys. Fluids* **6**, 973 (1994).
17. S. B. Pope, *PDF2DV: A Fortran Code to Solve the Modelled Joint PDF Equations for Two-Dimensional Turbulent Flows* (Cornell University, Ithaca, NY, 1994).

18. S. B. Pope, Particle method for turbulent flows: Integration of stochastic model equations, *J. Comput. Phys.* **117**, 332 (1995).
19. S. B. Pope, *Mean Field Equations in PDF Particle Method for Turbulent Reactive Flows*, Technical Report FDA 97-06 (Cornell University, Ithaca, NY, 1997).
20. S. B. Pope, *Turbulent Flows* (Cambridge Univ. Press, Cambridge, UK, 2000).
21. S. Subramaniam and S. B. Pope, Comparision of mixing model performance for nonpremixed turbulent reactive flow, *Combust. Flame* **117**, 732 (1999).
22. P. R. Van Slooten, Jayesh, and S. B. Pope, Advanced in PDF modeling for inhomogeneous turbulent flows, *Phys. Fluids* **10**, 246 (1998).
23. J. Xu and S. B. Pope, Assessment of numerical accuracy of PDF/Monte Carlo methods for turbulent reactive flows, *J. Comput. Phys.* **152**, 192 (1999).
24. J. Xu and S. B. Pope, *Source of Bias in Particle-Mesh Methods for PDF Models for Turbulent Flows*, Technical Report FDA 97-01 (Cornell University, Ithaca, NY, 1997).